

# A JOINT RECONSTRUCTION AND LAMBDA TOMOGRAPHY REGULARIZATION TECHNIQUE FOR ENERGY-RESOLVED X-RAY IMAGING

07/05/2022 12:50

JAMES WEBBER, ERIC TODD QUINTO, AND ERIC L. MILLER

ABSTRACT. Here we present new joint reconstruction and regularization techniques inspired by ideas in microlocal analysis and lambda tomography, for the simultaneous reconstruction of the attenuation coefficient and electron density from X-ray transmission (i.e., X-ray CT) and backscattered data (assumed to be primarily Compton scattered). To demonstrate our theory and reconstruction methods, we consider the “parallel line segment” acquisition geometry of [43], which is motivated by system architectures currently under development for airport security screening. We first present a novel microlocal analysis of the parallel line geometry which explains the nature of image artefacts when the attenuation coefficient and electron density are reconstructed separately. We next introduce a new joint reconstruction scheme for low effective  $Z$  (atomic number) imaging ( $Z < 20$ ) characterized by a regularization strategy whose structure is derived from lambda tomography principles and motivated directly by the microlocal analytic results. Finally we show the effectiveness of our method in combating noise and image artefacts on simulated phantoms.

## 1. INTRODUCTION

In this paper we introduce new joint reconstruction and regularization techniques based on ideas in microlocal analysis and lambda tomography [7, 8] (see also [26] for related work). We consider the simultaneous reconstruction of the target attenuation coefficient and electron density in X-ray ray imaging applications, with particular focus on the parallel line segment scanning geometry displayed in figures 1 and 2, which has the capability to measure transmission and Compton scattered data simultaneously. The acquisition geometry in question is based on a new airport baggage scanner currently in development. The parallel line geometry was first considered in [43], where injectivity results and explicit inversion formulae are derived for the Compton tomography problem. We provide an analysis of the stability of the Compton tomography problem here, from a microlocal perspective. The scanner consists of a fixed row of monochromatic fan beam sources ( $S$ ), a parallel row of detectors ( $D_A$ ) to measure the count of transmission photons, and a second (slightly out of plane) row of detectors ( $D_C$ ) to measure the Compton scattered intensity. Both sets of detectors are assumed to energy-resolved, as is commonly the case in Compton tomography [29, 40, 35, 36, 44], and the fan beam source opening angle is assumed to be  $\pi$  so there are no restrictions due to cropped fan beams.

The attenuation coefficient relates to the X-ray transmission data by the Beer-Lambert law [25, page 2]

$$(1.1) \quad \log \left( \frac{I_0}{I_A} \right) = \int_L \mu_E dl,$$

where  $I_A$  is the measured photon intensity at the detector (a point on  $D_A$ ),  $I_0$  is the initial source intensity and  $\mu_E$  is the attenuation coefficient at energy  $E$ . Here  $L$  is a line through a source and a detector points (a line through points on  $S$  and  $D_A$ ), with arc measure  $dl$ . With the full array of X-ray sources and detectors along  $S$  and  $D_A$  respectively, the transmission data determine a set of integrals of  $\mu_E$  over lines, and the problem of reconstructing  $\mu_E$  is formulated as an inversion of the line Radon transform with limited data (e.g., [25, 27]). Note that we need not account for the energy dependence of  $\mu_E$  in this case as the detectors are energy-resolved, so we have access to  $\int_L \mu_E ds$  data for any  $E$  in our energy range, and we can neglect any errors due to beam hardening effects. See figure 1.

When the attenuation of the incoming and scattered rays is ignored, the Compton scattered intensity in two dimensions can be modelled as the integrals of the electron density over toric sections [29, 40, 44]

$$(1.2) \quad I_C = \int_T n_e dt,$$

where  $I_C$  is the Compton scattered intensity measured at a point along  $D_C$  and  $n_e$  is the electron density. A toric section  $T = C_1 \cup C_2$  is the union of two intersecting circles of the same radii (as displayed in figure 1, see also [44]), and  $dt$  is the arc measure on  $T$ . Here the recovery of  $n_e$  is obtained by an inversion of the toric section (or circular arc) Radon transform [28, 29, 40, 44] (in the cited works a variety of source-detector acquisition geometries are considered for the toric section transform). See figure 2. See also [35, 36] for alternative reconstruction methods. Regarding the approximation made above to neglect the attenuative effects from the forward Compton model. When the attenuation effects are included, the inverse scattering problem becomes non-linear. We choose to focus on the analysis of the idealised linear case here, as this allows us to apply the well established theory on linear Fourier integral operators and microlocal analysis to derive a closed form expression for the image artefacts. Such analysis will likely give valuable insight into the image artefacts in the non-linear case moving forward. Furthermore, given the linear formulation, we can clearly demonstrate our theory in simulation through the application of linear least squares algorithms (so we do not face problems in the machinery of a non-linear inversion). The non-linear models and their inversion properties are hence left for future work.

The line and circular arc Radon transforms with full data (e.g. full fan beam transmission data [24] or the acquisition geometry of Palamodov for Compton data [29]), are known to have stable inverses in the sense that the solution for  $\mu_E$  and  $n_e$  is stable in some Sobolev space, and hence with adequate regularization we can reconstruct a density image free of artefacts. With limited data however (e.g. in the parallel line scanning geometry of figure 1, with limited angle transmission data [25], or limited energy Compton data [40]), the solution is unstable and the image wavefront set (the image edges and the directions in which they occur, see Definition 2.2) is not recovered stably in all directions. We will see later in section 3 through simulation that such data limitations in the parallel line geometry cause a blurring artefact over a cone in the reconstruction. There may also be additional non-local artefacts specific to the acquisition geometry (e.g. in [44] for Compton data), which we shall discover later in section 3 for Compton data in the parallel line scanner geometry.

The main goal of this paper is to combine limited datasets in transmission and Compton tomography with new lambda tomography regularization techniques, so as to be able to recover the image edges stably in all directions, with particular focus on the limited data

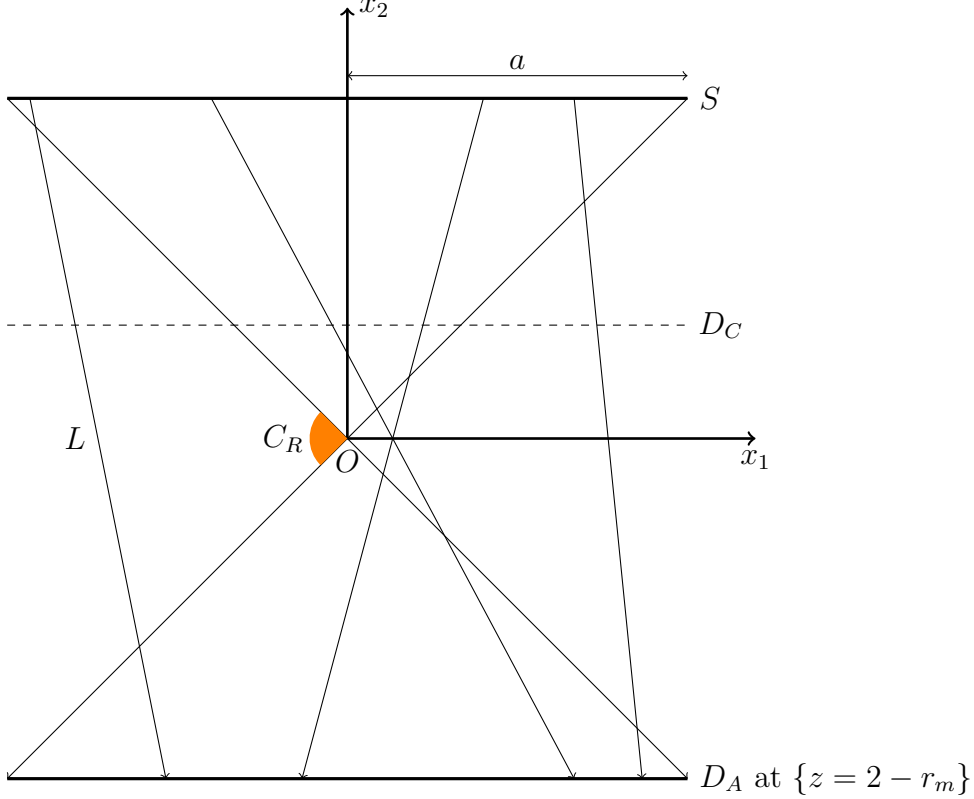


FIGURE 1. Parallel line X-ray transmission scanning geometry. Here  $S$ ,  $D_C$  and  $D_A$  denote a row of sources, scattering detectors and transmission detectors respectively. Since the fan beams are assumed to have opening angle  $\pi$ , the measured data correspond to the set of integrals of  $\mu_E$  over lines  $L$  which intersect the line segments  $S$  and  $D_A$  simultaneously. The length of the detector (and source) array is  $2a$ . An open cone of directions  $C_R \subset S^1$  is highlighted in orange. We will refer to  $C_R$  later for visualisation in section 4.

inherent to the parallel line scanner in figure 1. In lambda tomography the image reconstruction is carried out by filtered backprojection of the Radon projections, where the filter is chosen so as to provide an explicit solution modulo smoothing. This means that the jump singularities in the lambda reconstruction have the same location and direction to those of the target function, but the smooth parts are undetermined. A common choice of filter is a second derivative in the linear variable [4, 36]. The application of the derivative filter emphasizes the singularities in the Radon projections, and this is a key idea behind lambda tomography [7, 8, 41], and the microlocal view on lambda CT (e.g., [4, 33, 36]). The regularization penalty we propose aims to enforce a similarity in the wavefront sets of  $\mu_E$  and  $n_e$ , by minimizing the difference  $\|\frac{d^m}{ds^m} R(\mu_E - n_e)\|_{L^2(\mathbb{R} \times S^1)}$  for some  $m \geq 1$ , where  $R$  denotes the hyperplane Radon transform. Therefore, with a full set of Radon projections, the proposed regularization penalty enforces a similarity in the locations and magnitude of the image singularities (edges) of  $\mu_E$  and  $n_e$  in all directions. Furthermore  $\frac{d^m}{ds^m} R$  for  $m \geq 1$  is equivalent to taking  $m - 1/2$  derivatives of the object (this operation is continuous of positive order

$m - 1/2$  in Sobolev scales), and hence its inverse is a smoothing operation, which we expect to be of aid in combatting the measurement noise. In addition, the regularized inverse problem we propose is linear (similarly to the Tikhonov regularized inverse [15, page 99]), which (among other benefits of linearity) allows for the fast application of iterative least squares solvers in the solution. The linear least squares formulation is possible given the linearity of  $\frac{d^m}{ds^m}R$ .

Similar problems in joint image reconstruction and material characterization are considered in for example, [1, 14, 34, 37, 38, 39], and also regularization techniques for joint reconstruction methods in [3, 39]. In [37] the authors consider the joint reconstruction of the attenuation coefficient across multiple energies (a problem in hyperspectral or colour X-ray CT) from energy resolved transmission data. The reconstruction methods applied assume the attenuation maps to be highly correlated across energies and the authors develop low-rank tensor regularization schemes. The objective functions are non-linear and non-convex and the minimization is achieved using an Alternating Direction Method of Multipliers (ADMM) implementation. In [38] the authors consider the joint reconstruction of the photoelectric and Compton components of the attenuation coefficient from energy resolved data. Here the authors assume a similarity in the image wavefront sets (image edges), and enforce an edge similarity via a correlation type metric on the image gradients in the regularization. A satisfactory recovery of the Compton component is achieved using a Levenberg-Marquardt algorithm. However the recovery and regularization of the photoelectric component proved more troublesome. The regularization applied uses similar ideas to that of the cross-gradient constraints applied in [10, 11] in seismic imaging. The main difference being that the works of [10, 11] enforce the hard constraint that the image gradients must be parallel (or have cross product zero), whereas in [38] the constraints are soft and added as an additional objective penalty (which favours more highly correlated image gradients).

In [43] the authors introduce a new toric section transform  $\mathcal{T}$  in a translational geometry based on the machine scanner of figure 2. Here injectivity results, boundedness proofs and explicit inversion formulae are derived, but the stability analysis is lacking. We aim to address the stability of  $\mathcal{T}$  in this work from a microlocal perspective and, through an analysis of the canonical relations of  $\mathcal{T}$ , we discover the existence of non-local artefacts in the inversion, similarly to the works of [44]. In [34] the joint reconstruction of the attenuation coefficient and electron density in a pencil beam scanner geometry is considered. Here a gradient descent solver is applied to a non-linear objective function, derived from the physical models, and a weighted, iterative Tikhonov regularization penalty is applied. The works of [3] improve the wavefront set recovery in limited angle CT using a partially learned hybrid reconstruction scheme, which adopts ideas in microlocal analysis, machine learning and deep neural networks. However the fusion with Compton data is not considered. In our work we assume an equality in the image wavefront sets of the attenuation and electron density image (similarly to [38]), and we investigate the microlocal advantages of combining Compton and transmission data, as such an analysis is lacking in the literature. We introduce a new linear least squares problem for the joint recovery of the attenuation coefficient and electron density, with the aim to improve the recovery of the wavefront set of  $\mu_E$  and  $n_e$  simultaneously (in a similar vein to the cross-gradient methods of [10, 11] and the correlation penalties of [38]).

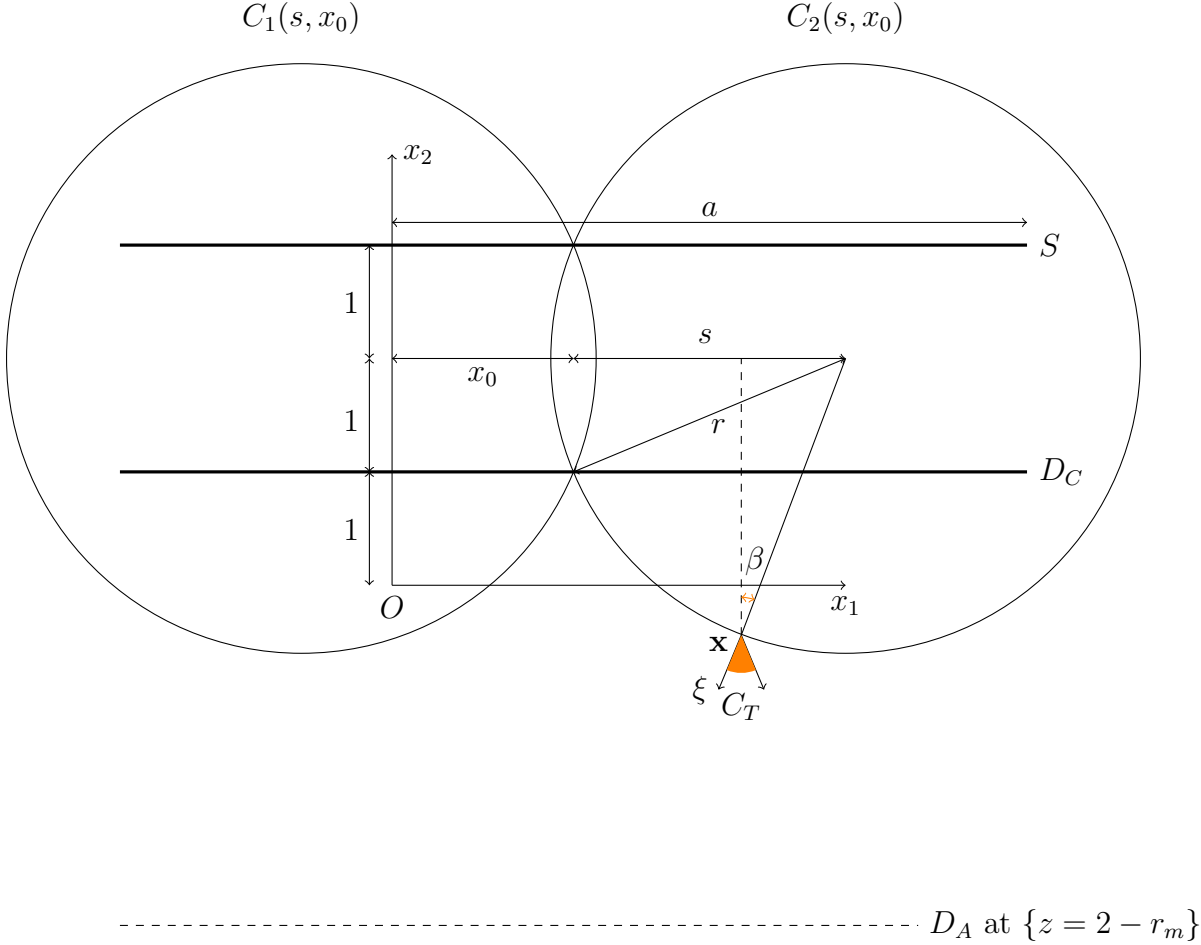


FIGURE 2. Parallel line Compton scanning geometry. Here  $S$ ,  $D_C$  and  $D_A$  denote a row of sources, scattering detectors and transmission detectors respectively. The remaining labels are referenced in the main text. The measured data correspond to the set of integrals over toric sections  $T = C_1 \cup C_2$  whose points of self intersection lie on the line segments  $S$  and  $D_C$ . An open cone of directions  $C_T \subset S^1$  is highlighted in orange. We will refer to  $C_T$  later for visualisation in section 3. Note that we have cropped out part of the left side (left of  $O$ ) of the scanner in this picture.

Using microlocal analysis, we will show how the data measured at the transmission and scattering detectors ( $D_A$  and  $D_C$  respectively, as labelled in figure 1) are highly complementary in terms of the image wavefront set recovery, and we later go on to demonstrate through simulation the significance of our microlocal theorems to the edge recovery of  $\mu_E$  and  $n_e$ . Under the assumption that the  $\mu_E$  and  $n_e$  images share the same wavefront information (i.e.  $\text{WF}(\mu_E) = \text{WF}(n_e)$ ), we derive a new regularization method based on ideas in lambda tomography which enforces a similarity between  $\text{WF}(\mu_E)$  and  $\text{WF}(n_e)$  in the joint reconstruction, while also applying a degree of smoothing, so as to combat the noise.

The remainder of this paper is organized as follows. In section 2, we recall some definitions and theorems from microlocal analysis which will be used to prove our theoretical results.

In section 3 we present a novel microlocal analysis of the toric section Radon transform  $\mathcal{T}$  in the parallel line geometry (to explain the image artefacts in a reconstruction of  $n_e$  from Compton data). Here we show that the toric section operator can be written as the sum of two Fourier Integral Operators (FIO's)  $\mathcal{T} = \mathcal{T}_1 + \mathcal{T}_2$ , where  $\mathcal{T}_1$  and  $\mathcal{T}_2$  are circular Radon transforms, which define the integrals of a function over circles with centers on a line. Through an analysis of the canonical relations  $\mathcal{C}_j$  of the  $\mathcal{T}_j$ , we provide proof that  $\mathcal{C}_j$  is 1–1. Following these results, we go on to prove our main theorem (Theorem 3.2), where we show that the canonical relation of  $\mathcal{T}$  (namely  $\mathcal{C}_1 \cup \mathcal{C}_2$ ) is 2–1. This implies the existence of non-local image artefacts in a reconstruction from toric section integral data. Further we find explicit expressions for the non-local artefacts and simulate these by applying the normal operations  $\mathcal{T}^*\mathcal{T}$  and  $\mathcal{T}_i^*\mathcal{T}_j$  (for  $i, j \in \{1, 2\}$ ) to a delta function (as in [44]) to demonstrate our theory.

In section 4 we present a microlocal analysis of the line Radon transform in the parallel line geometry in order to describe the artefacts in a reconstruction of  $\mu_E$  from transmission data. This amounts to a limited dataset for the line transform, whereby we have knowledge of  $\int_L \mu_E ds$  for all  $L$  which intersect the two line segments  $S$  and  $D_A$  (as in figure 1). The limited dataset we consider is shown to be described by a smooth “diamond-shaped” cutoff region of the full Radon sinogram (see figure 6) and hence is a special case of [2].

In section 5, we introduce our new joint reconstruction method for low effective  $Z$  imaging ( $Z < 20$ ) which combines the transmission and Compton data to reconstruct  $\mu_E$  and  $n_e$  simultaneously while enforcing a similarity in the image wavefront sets by lambda tomography regularization. Later in section 5 we present reconstructions of  $\mu_E$  and  $n_e$  image phantoms from simulated data using the proposed joint reconstruction and regularization methods. For comparison, and to back up the theory presented in sections 3 and 4, we present reconstructions of  $\mu_E$  and  $n_e$  from separate (non-joint) data with Total Variation (TV) regularizers. We also compare against a joint reconstruction with TV to further highlight the advantages (and disadvantages) of the proposed lambda regularizers. A joint reconstruction with lambda regularizers is shown to offer an improved image quality and reconstruction error in some cases when compared to the joint and non-joint TV methods. The joint TV method is shown to perform well also and is optimal among the methods tested on more complex phantoms. The separate TV reconstructions are found to be heavily distorted by limited data image artefacts (as predicted by our microlocal theory). We see an almost complete removal of the image artefacts when using joint data.

## 2. MICROLOCAL DEFINITIONS

We next recall some definitions. For  $X$  an open subset of  $\mathbb{R}^n$ , let  $\mathcal{D}'(X)$  denote the vector space of distributions on  $X$ , and let  $\mathcal{E}'(X)$  denote the vector space of distributions with compact support contained in  $X$ .

**Definition 2.1** ([19, Definition 7.1.1]). For a function  $f$  in the Schwartz space  $\mathcal{S}(\mathbb{R}^n)$ , we define the Fourier transform and its inverse as

$$(2.1) \quad \begin{aligned} \mathcal{F}f(\xi) &= \int_{\mathbb{R}^n} e^{-i\mathbf{x}\cdot\xi} f(\mathbf{x}) d\mathbf{x}, \\ \mathcal{F}^{-1}f(\mathbf{x}) &= (2\pi)^{-n} \int_{\mathbb{R}^n} e^{i\mathbf{x}\cdot\xi} f(\xi) d\xi. \end{aligned}$$

We use the standard multi-index notation: if  $\alpha = (\alpha_1, \alpha_2, \dots, \alpha_n) \in \{0, 1, 2, \dots\}^n$  is a multi-index and  $f$  is a function on  $\mathbb{R}^n$ , then

$$\partial^\alpha f = \left(\frac{\partial}{\partial x_1}\right)^{\alpha_1} \left(\frac{\partial}{\partial x_2}\right)^{\alpha_2} \cdots \left(\frac{\partial}{\partial x_n}\right)^{\alpha_n} f.$$

We identify cotangent spaces on Euclidean spaces with the underlying Euclidean spaces so if  $X$  is an open subset of  $\mathbb{R}^n$ , then the cotangent space of  $X$  is identified

$$T^*(X) = X \times (\mathbb{R}^n \setminus \{\mathbf{0}\}).$$

If  $\phi = \phi$  is a function of  $(\mathbf{x}, \xi) \in X \times \mathbb{R}^N$  then we define the derivatives

$$d_{\mathbf{x}}\phi = \left(\frac{\partial\phi}{\partial x_1}, \frac{\partial\phi}{\partial x_2}, \dots, \frac{\partial\phi}{\partial x_n}\right), \quad d_\xi\phi = \left(\frac{\partial\phi}{\partial \xi_1}, \frac{\partial\phi}{\partial \xi_2}, \dots, \frac{\partial\phi}{\partial \xi_N}\right)$$

and  $d\phi(\mathbf{x}, \xi) = (d_{\mathbf{x}}\phi(\mathbf{x}, \xi), d_\xi\phi(\mathbf{x}, \xi)) \in \mathbb{R}^n \times \mathbb{R}^N$ .

The singularities of a function and the directions in which they occur are described by the wavefront set [6, page 16]:

**Definition 2.2.** Let  $X$  be an open subset of  $\mathbb{R}^n$  and let  $f$  be a distribution in  $\mathcal{D}'(X)$ . Let  $(\mathbf{x}_0, \xi_0) \in X \times (\mathbb{R}^n \setminus \{\mathbf{0}\})$ . Then  $f$  is smooth at  $\mathbf{x}_0$  in direction  $\xi_0$  if there exists a neighbourhood  $U$  of  $\mathbf{x}_0$  and  $V$  of  $\xi_0$  such that for every  $\phi \in C_0^\infty(U)$  and  $N \in \mathbb{R}$  there exists a constant  $C_N$  such that

$$(2.2) \quad \left| \widehat{(\phi f)}(\lambda\xi) \right| \leq C_N (1 + |\lambda|)^{-N}.$$

The pair  $(\mathbf{x}_0, \xi_0)$  is in the wavefront set,  $\text{WF}(f)$ , if  $f$  is not smooth at  $\mathbf{x}_0$  in direction  $\xi_0$ .

This definition follows the intuitive idea that the elements of  $\text{WF}(f)$  are the point-normal vector pairs above points of  $X$  where  $f$  has singularities. For example if  $f$  is the characteristic function on the unit ball in  $\mathbb{R}^3$ , then

$$(2.3) \quad \text{WF}(f) = \{(\mathbf{x}, t\mathbf{x}) : \mathbf{x} \in S^2, t \neq 0\}.$$

That is, the wavefront set of the characteristic function on a ball is the set of points on a sphere paired with the normal vectors to the sphere.

The wavefront set of a distribution on  $X$  is normally defined as a subset of the cotangent bundle  $T^*(X)$  so it is invariant under diffeomorphisms, but we will not need this invariance. Therefore, we will continue with our identification of  $T^*(X) = X \times (\mathbb{R}^n \setminus \{\mathbf{0}\})$  and consider  $\text{WF}(f)$  as a subset of  $X \times \mathbb{R}^n \setminus \{\mathbf{0}\}$ .

**Definition 2.3** ([19, Definition 7.8.1]). Let  $X$  be an open subset of  $\mathbb{R}^n$ ,  $m \in \mathbb{R}$ . Then we define  $S^m(X \times \mathbb{R}^N)$  to be the set of  $a \in C^\infty(X \times \mathbb{R}^N)$  such that for every compact set  $K \subset X$  and all multi-indices  $\alpha, \beta$  the bound

$$\left| \partial_{\mathbf{x}}^\beta \partial_\xi^\alpha a(\mathbf{x}, \xi) \right| \leq C_{K, \alpha, \beta} (1 + |\xi|)^{m - |\alpha|}, \quad \mathbf{x} \in K, \quad \xi \in \mathbb{R}^n,$$

holds for some constant  $C_{K, \alpha, \beta} > 0$ . The elements of  $S^m$  are called *symbols* of order  $m$ .

Note that these symbols are sometimes denoted  $S_{1,0}^m$ .

**Definition 2.4** ([20, Definition 21.2.15]). A function  $\phi = \phi(\mathbf{x}, \xi) \in C^\infty(X \times \mathbb{R}^N \setminus \{\mathbf{0}\})$  is a *phase function* if  $\phi(\mathbf{x}, \lambda\xi) = \lambda\phi(\mathbf{x}, \xi)$ ,  $\forall \lambda > 0$  and  $d\phi$  is nowhere zero. A phase function is *clean* if the critical set  $\Sigma_\phi = \{(\mathbf{x}, \xi) : d_\xi\phi(\mathbf{x}, \xi) = 0\}$  is a smooth manifold with tangent space defined by  $d(d_\xi\phi) = 0$ .

By the implicit function theorem the requirement for a phase function to be clean is satisfied if  $d(d_\xi\phi)$  has constant rank.

**Definition 2.5** ([20, Definition 21.2.15] and [21, Section 25.2]). Let  $X \subset \mathbb{R}^{n_x}$ ,  $Y \subset \mathbb{R}^{n_y}$  be open sets. Let  $\phi \in C^\infty(Y \times X \times (\mathbb{R}^N \setminus \{\mathbf{0}\}))$  be a clean phase function. Then, the *critical set* of  $\phi$  is

$$\Sigma_\phi = \{(\mathbf{y}, \mathbf{x}, \xi) \in Y \times X \times \mathbb{R}^N \setminus \{\mathbf{0}\} : d_\xi\phi = 0\}.$$

In addition, we assume that  $\phi$  is *nondegenerate* in the following sense:

$$d_{\mathbf{y},\xi}\phi \text{ and } d_{\mathbf{x},\xi}\phi \text{ are never zero.}$$

The *canonical relation parametrised by  $\phi$*  is defined as

$$(2.4) \quad \mathcal{C} = \{((\mathbf{y}, d_{\mathbf{y}}\phi(\mathbf{y}, \mathbf{x}, \xi)), (\mathbf{x}, -d_{\mathbf{x}}\phi(\mathbf{y}, \mathbf{x}, \xi))) : (\mathbf{y}, \mathbf{x}, \xi) \in \Sigma_\phi\},$$

**Definition 2.6.** Let  $X \subset \mathbb{R}^{n_x}$ ,  $Y \subset \mathbb{R}^{n_y}$  be open sets. A Fourier integral operator (FIO) of order  $m + N/2 - (n_x + n_y)/4$  is an operator  $A : C_0^\infty(X) \rightarrow \mathcal{D}'(Y)$  with Schwartz kernel given by an oscillatory integral of the form

$$(2.5) \quad K_A(\mathbf{y}, \mathbf{x}) = \int_{\mathbb{R}^N} e^{i\phi(\mathbf{y}, \mathbf{x}, \xi)} a(\mathbf{y}, \mathbf{x}, \xi) d\xi,$$

where  $\phi$  is a clean nondegenerate phase function and  $a \in S^m(Y \times X \times \mathbb{R}^N)$  a symbol. The canonical relation of  $A$  is the canonical relation of  $\phi$  defined in (2.4).

This is a simplified version of the definition of FIO in [5, Section 2.4] or [21, Section 25.2] that is suitable for our purposes since our phase functions are global. For general information about FIOs see [5, 21, 20].

**Definition 2.7.** Let  $\mathcal{C} \in T^*(Y \times X)$  be the canonical relation associated to the FIO  $A : \mathcal{E}'(X) \rightarrow \mathcal{D}'(Y)$ . Then we denote  $\pi_L$  and  $\pi_R$  to be the natural left- and right-projections of  $\mathcal{C}$ ,  $\pi_L : \mathcal{C} \rightarrow T^*(Y) \setminus \{\mathbf{0}\}$  and  $\pi_R : \mathcal{C} \rightarrow T^*(X) \setminus \{\mathbf{0}\}$ .

We have the following result from [21].

**Proposition 2.8.** *Let  $\dim(X) = \dim(Y)$ . Then at any point in  $\mathcal{C}$ :*

- (i) *if one of  $\pi_L$  or  $\pi_R$  is a local diffeomorphism, then the other map is a local diffeomorphism (so  $\mathcal{C}$  is a local canonical graph);*
- (ii) *if one of the projections  $\pi_R$  or  $\pi_L$  is singular at a point in  $\mathcal{C}$ , then so is the other. The type of the singularity may be different but both projections drop rank on the same set*

$$(2.6) \quad \Sigma = \{(\mathbf{y}, \eta; \mathbf{x}, \xi) \in \mathcal{C} : \det(d\pi_L) = 0\} = \{(\mathbf{y}, \eta; \mathbf{x}, \xi) \in \mathcal{C} : \det(d\pi_R) = 0\}.$$

If a FIO  $\mathcal{F}$  satisfies our next definition, then  $\mathcal{F}^*\mathcal{F}$  (or  $\mathcal{F}^*\phi\mathcal{F}$  if  $\mathcal{F}$  does not map to  $\mathcal{E}'(Y)$ ) is a pseudodifferential operator [13, 31].

**Definition 2.9.** Let  $\mathcal{F} : \mathcal{E}'(X) \rightarrow \mathcal{D}'(Y)$  be a FIO with canonical relation  $\mathcal{C}$  then  $\mathcal{F}$  (or  $\mathcal{C}$ ) satisfies the *semi-global Bolker Assumption* if the natural projection  $\pi_Y : \mathcal{C} \rightarrow T^*(Y)$  is an embedding (injective immersion).



### 3. MICROLOCAL PROPERTIES OF TRANSLATIONAL COMPTON TRANSFORMS

Here we present a microlocal analysis of the toric section transform in the translational (parallel line) scanning geometry. Through an analysis of two separate limited data problems for the circle transform (where the integrals over circles with centres on a straight line are known) and using microlocal analysis, we show that the canonical relation of the toric section transform is 2–1. The analysis follows in a similar way to the work of [44].

Let  $r_m > 1$  and define the set of points to be scanned as

$$X := \{(x_1, x_2) \in \mathbb{R}^2 : 2 - r_m < x_2 < 1\}.$$

Here  $r_m$  controls the depth of the scanning tunnel as in figures 1 and 2.

Let  $(s, x_0) \in Y := (0, \infty) \times \mathbb{R}$ . For  $j = 1, 2$  we define the circles  $C_j$  and their centers  $\mathbf{c}_j$

$$(3.1) \quad \begin{aligned} r &= \sqrt{s^2 + 1}, \quad \mathbf{c}_j(s, x_0) = ((-1)^j s + x_0, 2) \\ C_j(s, x_0) &= \{\mathbf{x} \in \mathbb{R}^2 : |\mathbf{x} - \mathbf{c}_j(s, x_0)|^2 - s^2 - 1 = 0\}. \end{aligned}$$

Note that  $r = \sqrt{s^2 + 1}$  is the radius of the circle  $C_j$ . The union of the reflected circles  $C_1 \cup C_2$  is called a *toric section*. Let  $f \in L_0^2(X)$  be the electron charge density. To define the toric section transform we first introduce two *circle transforms*

$$(3.2) \quad \mathcal{T}_1 f(s, x_0) = \int_{C_1} f ds, \quad \mathcal{T}_2 f(s, x_0) = \int_{C_2} f ds.$$

Now we have the definition of the *toric section transform*

$$(3.3) \quad \mathcal{T} f(s, x_0) = \int_{C_1 \cup C_2} f ds = \mathcal{T}_1(f)(s, x_0) + \mathcal{T}_2(f)(s, x_0)$$

where  $ds$  denotes the arc element on a circle.

We express  $\mathcal{T}$  in terms of delta functions as is done for the generalized Funk-Radon transforms studied by Palamodov [30]

$$(3.4) \quad \begin{aligned} \mathcal{T} f(s, x_0) &= \mathcal{T}_1 f(s, x_0) + \mathcal{T}_2 f(s, x_0) \\ &= \frac{1}{2r} \sum_{j=1}^2 \int_{\mathbb{R}^2} \delta(|\mathbf{x} - \mathbf{c}_j(s, x_0)|^2 - s^2 - 1) f(\mathbf{x}) d\mathbf{x} \\ &= \frac{1}{2r} \sum_{j=1}^2 \int_{\mathbb{R}^2} \delta(|\mathbf{x} - ((-1)^j s + x_0, 2)|^2 - s^2 - 1) f(\mathbf{x}) d\mathbf{x} \\ &= \frac{1}{2r} \sum_{j=1}^2 \int_{-\infty}^{\infty} \int_{\mathbb{R}^2} e^{-i\sigma(|\mathbf{x} - ((-1)^j s + x_0, 2)|^2 - s^2 - 1)} f(\mathbf{x}) d\mathbf{x} d\sigma. \end{aligned}$$

Note that the factor in front of the integrals comes about using the change of variables formula and that  $\mathcal{T}_j f = \int \delta(|\mathbf{x} - \mathbf{c}_j(s, x_0)| - \sqrt{s^2 + 1}) f(x) d\mathbf{x}$ . So the toric section transform is the sum of two FIO's with phase functions

$$\phi_j(s, x_0, \mathbf{x}, \sigma) = \sigma(|\mathbf{x} - ((-1)^j s + x_0, 2)|^2 - s^2 - 1)$$

for  $j = 1, 2$ . Our distributions  $f$  are supported away from the intersection points of  $C_1$  and  $C_2$ , and hence we can consider the microlocal properties of  $\mathcal{T}_1$  and  $\mathcal{T}_2$  separately to describe the microlocal properties of  $\mathcal{T}$ .

**Proposition 3.1.** *For  $j = 1, 2$ , the circle transform  $\mathcal{T}_j$  is an FIO of order  $-1/2$  with canonical relation*

$$(3.5) \quad \mathcal{C}_j = \left\{ (s, x_0, (-1)^{j-1}\sigma(x_1 - x_0), -\sigma((-1)^{j-1}s + x_1 - x_0); \mathbf{x}, -\sigma(\mathbf{x} - \mathbf{c}_j(s, x_0))) : (s, x_0) \in Y, \sigma \in \mathbb{R} \setminus \{0\}, \mathbf{x} \in C_j(s, x_0) \cap \{x_2 < 1\} \right\}.$$

Furthermore  $\mathcal{C}_j$  satisfies the semi-global Bolker assumption for  $j = 1, 2$ .

*Proof.* First, one can check that  $\phi_j$  and  $\mathcal{T}_j$  both satisfy the restrictions in Definition 2.6 so  $\mathcal{T}_j$  is a FIO. Using this definition again and the fact that its symbol is order zero [31], one sees that it has order  $-1/2$ .

A straightforward calculation using Definition 2.5 shows that the canonical relation of  $\mathcal{T}_j$  is as given in (3.5). Note that we have absorbed a factor of 2 into  $\sigma$  in this calculation.

Note that coordinates on  $\mathcal{C}_j$  are given by

$$(3.6) \quad \begin{aligned} (s, x_0, x_1, \sigma) &\mapsto (s, x_0, (-1)^{j-1}\sigma(x_1 - x_0), -\sigma((-1)^{j-1}s + x_1 - x_0); \\ &(x_1, x_2), -\sigma((x_1, x_2) - \mathbf{c}_j(s, x_0))) \\ &\text{where } x_2 = 2 - \sqrt{s^2 + 1 - (x_1 - (x_0 + (-1)^j s))^2} \end{aligned}$$

because  $x_2 < 1$ . Note that  $\mathbf{c}_j$  is given in (3.1).

We now show that  $\mathcal{C}_j$  satisfies the semiglobal Bolker assumption by finding a smooth inverse in these coordinates to the projection  $\Pi_L : \mathcal{C}_j \rightarrow T^*(Y)$ . Let  $\lambda = (s, x_0, \tau_1, \tau_2) \in \Pi_L(\mathcal{C}_j)$ . We solve for  $x_1$  and  $\sigma$  in the equation  $\Pi_L(s, x_0, x_1, \sigma) = \lambda$ . First,  $s$  and  $x_0$  are known and

$$(3.7) \quad \begin{aligned} \tau_1 &= (-1)^{j-1}\sigma(x_1 - x_0) \\ \tau_2 &= -\sigma((-1)^{j-1}s + x_1 - x_0). \end{aligned}$$

A straightforward linear algebra exercise shows that the unique solutions for  $\sigma$  and  $x_1$  are

$$(3.8) \quad \sigma = \frac{(-1)^j \tau_2 - \tau_1}{s}, \quad x_1 = \frac{s\tau_1}{(-1)^j \tau_1 - \tau_2} + x_0$$

This gives a smooth inverse to  $\Pi_L$  on the image  $\Pi_L(\mathcal{C}_j)$  and finishes the proof.  $\square$

Because  $\mathcal{C}_j$  satisfies the Bolker Assumption, the composition  $\mathcal{C}_j^* \circ \mathcal{C}_j \subset \Delta$ , where  $\Delta$  is the diagonal in  $T^*(X)$ . Hence in a reconstruction from circular integral data with centres on a line we would not expect to see image artefacts for functions supported in  $x - 2 > 0$  unless one uses a sharp cutoff on the data.

The canonical relation  $\mathcal{C}$  of  $\mathcal{T}$  can be written as the disjoint union  $\mathcal{C} = \mathcal{C}_1 \cup \mathcal{C}_2$  (since  $(\mathcal{C}_1 \cap \mathcal{C}_2) \cap \text{supp}(f) = \emptyset$ ).

For convenience, we will sometimes label the coordinate  $x_0$  in (3.6) as  $(x_0)_1$  if it is associated with  $\mathcal{C}_1$  and  $(x_0)_2$  if it is associated with  $\mathcal{C}_2$ .

**Theorem 3.2.** *For  $j = 1, 2$ , the projection  $\Pi_R : \mathcal{C}_j \rightarrow T^*(X)$  is bijective onto the set*

$$(3.9) \quad D = \{(\mathbf{x}, \xi) \in T^*(X) : \xi_2 \neq 0\}.$$

In addition,  $\Pi_R : \mathcal{C} \rightarrow T^*(X)$  is two-to one onto  $D$ .

*Proof.* Let  $\mu = (\mathbf{x}; \xi) \in T^*(X) \setminus \{\mathbf{0}\}$  and let  $\mathbf{x} = (x_1, x_2)$  and  $\xi = (\xi_1, \xi_2)$ . If  $\mu \in \Pi_R(\mathcal{C}_j)$  for either  $j = 1$  or  $j = 2$ , then  $\xi_2 \neq 0$  by (3.5) since  $x_2 < 2$ . For the rest of the proof, assume  $\mu$  is in the set  $D$  given by (3.9)

We will now describe the preimage of  $\mu$  in  $\mathcal{C}_j$ . The covector  $\mu$  is conormal to a unique circle centered on  $x_2 = 2$ , and its center is on the line through  $\mathbf{x}$  and parallel  $\xi$ . If the center has coordinates  $(c, 2)$ , then a calculation shows that  $c$  is given by

$$(3.10) \quad c = c(\mathbf{x}, \xi) = x_1 - \frac{\xi_1(x_2 - 2)}{\xi_2}.$$

Using this calculation, one sees that the radius of the circle and coordinate  $s$  are given by

$$(3.11) \quad r = r(\mathbf{x}, \xi) = \frac{(2 - x_2)|\xi|}{|\xi_2|}, \quad s = s(\mathbf{x}, \xi) = \sqrt{r^2 - 1}$$

and the coordinate  $(x_0)_j$  is given by

$$(3.12) \quad (x_0)_j = (x_0)_j(\mathbf{x}, \xi) = x_1 + \frac{\xi_1(2 - x_2)}{\xi_2} + (-1)^{j-1}s \quad \text{for } j = 1, 2.$$

A straightforward calculation shows that

$$(3.13) \quad \sigma = \sigma(\mathbf{x}, \xi) = \frac{-\xi_2}{2 - x_2}.$$

This gives the coordinates (3.6) on  $\mathcal{C}_j$  and shows that  $\Pi_R : \mathcal{C}_j \rightarrow D$  is injective with smooth inverse.

Now, we consider the projection from  $\mathcal{C}$ . Given  $(\mathbf{x}, \xi) \in D$ , our calculations show that the preimage in  $\mathcal{C}$ , in coordinates (3.6) is given by two *distinct* points

$$(s(\mathbf{x}, \xi), (x_0)_j(\mathbf{x}, \xi), x_1, \sigma(\mathbf{x}, \xi)) \quad \text{for } j = 1, 2.$$

The coordinates are given by (3.11), (3.12) and (3.13) respectively. □

The abstract adjoint  $\mathcal{T}_j^t$  cannot be composed with  $\mathcal{T}_i$  for  $i = 1, 2$ , because the support of  $\mathcal{T}_i f$  can be unbounded in  $r$ , even for  $f \in \mathcal{E}'(X)$  and  $\mathcal{T}_j^t$  is not defined for such distributions. Therefore, we introduce a smooth cutoff function. Choose  $r_M > 2$  and let  $\psi$  be a smooth compactly supported function equal to one on  $[1, r_M]$  and define

$$(3.14) \quad \mathcal{T}_j^* g = \mathcal{T}_j^t(\psi g)$$

for all  $g \in \mathcal{D}'(Y)$  because our bound on  $r$  introduces a bound on  $x_0$  so the integral is over a bounded set.

Now, we can state our next theorem, which describes the artifacts that can be added to the reconstruction using the normal operator,  $\mathcal{T}^* \mathcal{T}$ .

**Theorem 3.3.** *If  $f \in \mathcal{E}'(X)$  then*

$$(3.15) \quad \text{WF}(\mathcal{T}^* \mathcal{T} f) \subset (\text{WF}(f) \cap D) \cup \Lambda_{12}(f) \cup \Lambda_{21}(f)$$

where  $D$  is given by (3.9), and the sets  $\Lambda_{ij}$  are given for  $(\mathbf{x}, \xi) \in D$  by

$$(3.16) \quad \Lambda_{ij}(f) = \{\lambda_{ij}(\mathbf{x}, \xi) : (\mathbf{x}, \xi) \in \text{WF}(f) \cap D\}$$

where the functions  $\lambda_{12}$  and  $\lambda_{21}$  are given by (3.19) and (3.20) respectively. Note that the functions  $\lambda_{ij}$  are defined for only some  $(\mathbf{x}, \xi) \in D$  and singularities at other points do not generate artifacts.

Therefore,  $\mathcal{T}^*\mathcal{T}$  recovers most singularities of  $f$ , as indicated in the first term in (3.15), but it adds two sets of singularities, as given by  $\Lambda_{12}(f)$  and  $\Lambda_{21}(f)$ . Note that, even if  $\mathcal{T}_j^*$  and  $\mathcal{T}_j$  are both elliptic above a covector  $(\mathbf{x}, \xi)$ , artifacts caused by other points could mask singularities of  $f$  that “should” be visible in  $\mathcal{T}^*\mathcal{T}f$ .

*Proof.* Let  $f \in \mathcal{E}'(X)$ . By the Hörmander-Sato Lemma [19, Theorem 8.2.13] We have the expansion

$$\begin{aligned}
(3.17) \quad \text{WF}(\mathcal{T}^*\mathcal{T}(f)) &\subset (\mathcal{C}^* \circ \mathcal{C}) \circ \text{WF}(f) \\
&= [(\mathcal{C}_1^* \circ \mathcal{C}_1) \cup (\mathcal{C}_2^* \circ \mathcal{C}_2)] \circ \text{WF}(f) \\
&\quad \cup (\mathcal{C}_2^* \circ \mathcal{C}_1) \circ \text{WF}(f) \\
&\quad \cup (\mathcal{C}_1^* \circ \mathcal{C}_2) \circ \text{WF}(f)
\end{aligned}$$

The first term in brackets in (3.17) is  $\{(\mathbf{x}, \xi; \mathbf{x}, \xi) : (\mathbf{x}, \xi) \in D\} \circ \text{WF}(f) = \text{WF}(f) \cap D$ . This proves the first part of the inclusion (3.15).

We now analyze the other two terms to define the functions  $\lambda_{ij}$  and finish the proof. Let  $(\mathbf{x}, \xi) \in \text{WF}(f) \cap D$ . First, consider  $\lambda_{12}(\mathbf{x}, \xi) = \mathcal{C}_2^* \circ \mathcal{C}_1(\mathbf{x}, \xi)$ . Using the calculations in the proof of Theorem 3.2 one sees that  $\mathcal{C}_1 \circ (\mathbf{x}, \xi)$ <sup>1</sup> is given by

$$\begin{aligned}
(3.18) \quad (s, x_0, \tau_1, \tau_2) \quad \text{where} \quad s &= s(\mathbf{x}, \xi) = \sqrt{\frac{(2-x_2)^2 |\xi|^2}{\xi_2^2} - 1} \\
x_0 &= (x_0)_1(\mathbf{x}, \xi) = x_1 + \frac{\xi_1(2-x_2)}{\xi_2} + s \\
\sigma &= \sigma(\mathbf{x}, \xi) = \frac{-\xi_2}{2-x_2} \\
\tau_1 &= \sigma(x_1 - x_0) \quad \tau_2 = -\sigma(s + x_1 - x_0)
\end{aligned}$$

where we have taken these from the proof of Theorem 3.2. To find  $\mathcal{C}_2^* \circ \mathcal{C}_1 \circ (\mathbf{x}, \xi)$  we calculate the composition of the covector described in (3.18) with  $\mathcal{C}_2^*$ . Note that the values of  $x_0$  and  $s$  are the same in both calculations and are given by (3.18). After using (3.8) and that  $\frac{\xi_1(2-x_2)}{\xi_2} = x_0 - s - x_1$ , one sees that

$$\begin{aligned}
(3.19) \quad \lambda_{12}(\mathbf{x}, \xi) &= ((y_1, y_2), \eta) \quad \text{where} \\
y_1 &= y_1(\mathbf{x}, \xi) = \frac{s(x_1 - x_0)}{2(x_1 - x_0) + s} + x_0 \\
y_2 &= y_2(\mathbf{x}, \xi) = 2 - \sqrt{\frac{(2-x_2)^2 |\xi|^2}{\xi_2^2} - (y_1 - (x_0 + s))^2} \\
\eta &= \left( -2\xi_1 - \frac{s\xi_2}{2-x_2} \right) (\mathbf{y} - \mathbf{c}_2(s(\mathbf{x}, \xi)(x_0)_1(\mathbf{x}, \xi)))
\end{aligned}$$

where  $x_0 = (x_0)_1(\mathbf{x}, \xi)$  and  $s = s(\mathbf{x}, \xi)$  are given in (3.18) and  $\eta$  is calculated using the expression (3.8) with  $j = 2$ .

<sup>1</sup>For convenience, we will abbreviate the set theoretic composition  $\mathcal{C}_i \circ \{(\mathbf{x}, \xi)\}$  by  $\mathcal{C}_i \circ (\mathbf{x}, \xi)$ .

Note that the function  $\lambda_{12}$  is defined for only some  $(\mathbf{x}, \xi) \in D$ ; for example if the argument for the square root defining  $y_2(\mathbf{x}, \xi)$  is negative, then  $y_2(\mathbf{x}, \xi)$  is not defined and the point  $(\mathbf{x}, \xi)$  will not generate artifacts in  $\Lambda_{12}$ .

A similar calculation shows for  $(\mathbf{y}, \eta) \in D$  that

$$(3.20) \quad \begin{aligned} \lambda_{21}(\mathbf{y}, \eta) &= ((x_1, x_2), \xi) \quad \text{where} \\ x_1 = x_1(\mathbf{y}, \eta) &= \frac{s(y_1 - x_0)}{-2(y_1 - x_0) + s} + x_0 \\ x_2 = x_2(\mathbf{y}, \eta) &= 2 - \sqrt{s^2(\mathbf{y}, \eta) + 1 - (x_1 - (x_0 - s))^2} \\ \xi &= \left( 2\eta_1 - \frac{s\eta_2}{2 - y_2} \right) (\mathbf{x} - \mathbf{c}_1(s(\mathbf{y}, \eta), (x_0)_2(\mathbf{y}, \eta))) \end{aligned}$$

where

$$\begin{aligned} s = s(\mathbf{y}, \eta) &= \sqrt{\frac{(2 - y_2)^2 |\eta|^2}{\eta_2^2} - 1} \\ x_0 = (x_0)_2(\mathbf{y}, \eta) &= y_1 + \frac{\eta_1(2 - y_2)}{\eta_2} - s. \end{aligned}$$

Note that the function  $\lambda_{21}$  is not defined for all  $(\mathbf{y}, \eta) \in D$ , and other points  $(\mathbf{y}, \eta)$  do not generate artifacts. This is for the same reason as for  $\lambda_{12}$ .  $\square$

*Remark 3.4.* The artefacts caused by a singularity of  $f$  are as strong as the reconstruction of that singularity.

First note that each  $\mathcal{T}_j^* \mathcal{T}_i$  smooths of order one in Sobolev scale since it an FIO of order  $-1$  [18, Theorem 4.3.1].

The visible singularities in the reconstruction come from the compositions  $\mathcal{T}_1^* \mathcal{T}_1$  and  $\mathcal{T}_2^* \mathcal{T}_2$  since these are pseudodifferential operators of order  $-1$ . The artefacts come from the ‘‘cross’’ compositions  $\mathcal{T}_2^* \mathcal{T}_1$  and  $\mathcal{T}_1^* \mathcal{T}_2$ , and they are FIO of order  $-1$ . Therefore, since the terms that preserve the real singularities of  $f$ ,  $\mathcal{T}_i^* \mathcal{T}_i$ ,  $i = 1, 2$ , are also of order  $-1$ ,  $\mathcal{T}^* \mathcal{T}$  smooths each singularity of  $f$  by one order in Sobolev scale *and* the composition  $\mathcal{T}_2^* \mathcal{T}_1$  (corresponding to the artifact  $\lambda_{12}$ , if defined at this covector) can create an artefact from that singularity that are also one order smoother than that singularity, and similarly with the composition  $\mathcal{T}_1^* \mathcal{T}_2$ .

Second, our results are valid, not only for the normal operator  $\mathcal{T}^* \mathcal{T}$  but for any filtered backprojection method  $\mathcal{T}^* P \mathcal{T}$  where  $P$  is a pseudodifferential operator. This is true since pseudodifferential operators have canonical relation  $\Delta$  and they do not move singularities, so our microlocal calculations are the same. If  $P$  has order  $k$ , then  $\mathcal{T}^* P \mathcal{T}$  decreases the Sobolev order of each singularity of  $f$  by order  $(k - 1)$  in Sobolev norm and can create an artefact from that singularity of the same order.

**3.1. Artifacts for  $\mathcal{T}^* \mathcal{T}$  due to limited data.** In practice we do not have access to  $\mathcal{T}f(s, x_0)$  for all  $s \in (0, \infty)$  (or  $r \in (1, \infty)$ ) and  $x_0 \in \mathbb{R}$ , and will have knowledge of  $x_0 \in (-a, a)$  and  $r \in (1, r_M)$  for some  $a > 0$  (see figures 1 and 2) and maximum radius  $r_M > 1$ .

We now evaluate which wavefront directions  $(\mathbf{x}, \xi)$  will be visible from this limited data. Let us consider the pair  $(\mathbf{x}, \xi) \in C_2(s, x_0) \times S^1$  and let  $\beta$  be the angle of  $\xi$  from the vertical

as depicted in figure 2. Then  $\mathbf{c}_2(s, x_0) = ((2 - x_2) \tan \beta + x_1, 2)$  and

$$|\mathbf{x} - \mathbf{c}_2(s, x_0)|^2 = r^2 \implies (1 + \tan^2 \beta)(2 - x_2)^2 = r^2 \implies \tan \beta = \sqrt{\frac{r^2}{(2 - x_2)^2} - 1}.$$

Let  $\beta_m = \beta_m(\mathbf{x}) \in (0, \pi/2)$  be defined by

$$(3.21) \quad \tan \beta_m = \sqrt{\frac{r_M^2}{(2 - x_2)^2} - 1}$$

(noting that we only consider  $\mathbf{x}$  such that  $1 > x_2 > 2 - r_M$ ). Then the maximum directional coverage of the singularities (wavefront set) at a given  $\mathbf{x} \in X$  which are resolved by the Compton data are described by the open cone of  $\xi \in S^1$

$$(3.22) \quad C_T = \{\pm(\sin \beta, -\cos \beta) : -\beta_m < \beta < \beta_m\},$$

and the opening angle of the cone depends on the depth of  $\mathbf{x}$  (i.e.  $x_2$ ). See figure 2. The cone  $C_T$  illustrated corresponds to the case when  $\beta = \beta_m$ .

In all of our numerical experiments, we set the tunnel height as  $r_m - 1 = 6$  and the detector line width is  $2a = 8$ . We let  $r_M > r_m$  be large enough to penetrate the entire scanning tunnel (up to the line  $\{x_2 = 2 - r_m\}$  as highlighted in figures 1 and 2), so as to imply a unique reconstruction [44]. Specifically we set the maximum radius  $r_M = 9$  and simulate  $\mathcal{T}(r, x_0)$  for  $r \in \{1 + 0.02j : 1 \leq j \leq 400\}$  and  $x_0 \in \{-4 + 0.04j : 1 \leq j \leq 200\}$ . Further the densities considered are represented on  $[-2, 2] \times [-3, 1]$  ( $200 \times 200$  pixel grid) in the reconstructions shown. The machine design considered is such that for any  $\mathbf{x} \in [-2, 2] \times [-1.5, 1]$  we have the maximal directional coverage in  $C_T$  allowed for the limited  $r < r_M$  (see figure 8). With the exception of the horizontal bar phantom depicted in figure 13, all objects considered for reconstruction are approximately in this region.

To demonstrate the artefacts, we apply a discrete form of  $\mathcal{T}^*\mathcal{T}$  to a delta function. We have the expansion

$$(3.23) \quad \begin{aligned} \mathcal{T}^*\mathcal{T} &= (\mathcal{T}_1 + \mathcal{T}_2)^*(\mathcal{T}_1 + \mathcal{T}_2) \\ &= \mathcal{T}_1^*\mathcal{T}_1 + \mathcal{T}_2^*\mathcal{T}_2 + \mathcal{T}_1^*\mathcal{T}_2 + \mathcal{T}_2^*\mathcal{T}_1. \end{aligned}$$

Using equations (3.18), (3.19), and (3.20) we can define the backprojection operators  $\mathcal{T}_1^*$  and  $\mathcal{T}_2^*$

$$(3.24) \quad \mathcal{T}_1^*g(\mathbf{x}) = \int_{-\beta_m}^{\beta_m} g\left(\sqrt{r^2 - 1}, x_1 + \sqrt{r^2 - 1} + r \sin \beta\right) \Big|_{r=\frac{(2-x_2)}{\cos \beta}} d\beta$$

and

$$(3.25) \quad \mathcal{T}_2^*g(\mathbf{x}) = \int_{-\beta_m}^{\beta_m} g\left(\sqrt{r^2 - 1}, x_1 - \sqrt{r^2 - 1} + r \sin \beta\right) \Big|_{r=\frac{(2-x_2)}{\cos \beta}} d\beta.$$

Now, let  $f$  be a delta function at  $\mathbf{y}$ . We calculate the artifacts

$$(3.26) \quad \mathcal{T}_1^*\mathcal{T}_2f(\mathbf{x}) \neq 0 \iff \exists \beta \in [-\beta_m, \beta_m] \text{ s.t. } |\mathbf{y} - \mathbf{c}_2(s, x_0)| = r,$$

where  $r = \frac{2-x_2}{\cos \beta}$ ,  $s = \sqrt{r^2 - 1}$  and  $x_0 = x_1 + s + r \sin \beta$ . Similarly

$$(3.27) \quad \mathcal{T}_2^*\mathcal{T}_1f(\mathbf{x}) \neq 0 \iff \exists \beta \in [-\beta_m, \beta_m] \text{ s.t. } |\mathbf{y} - \mathbf{c}_1(s, x_0)| = r,$$

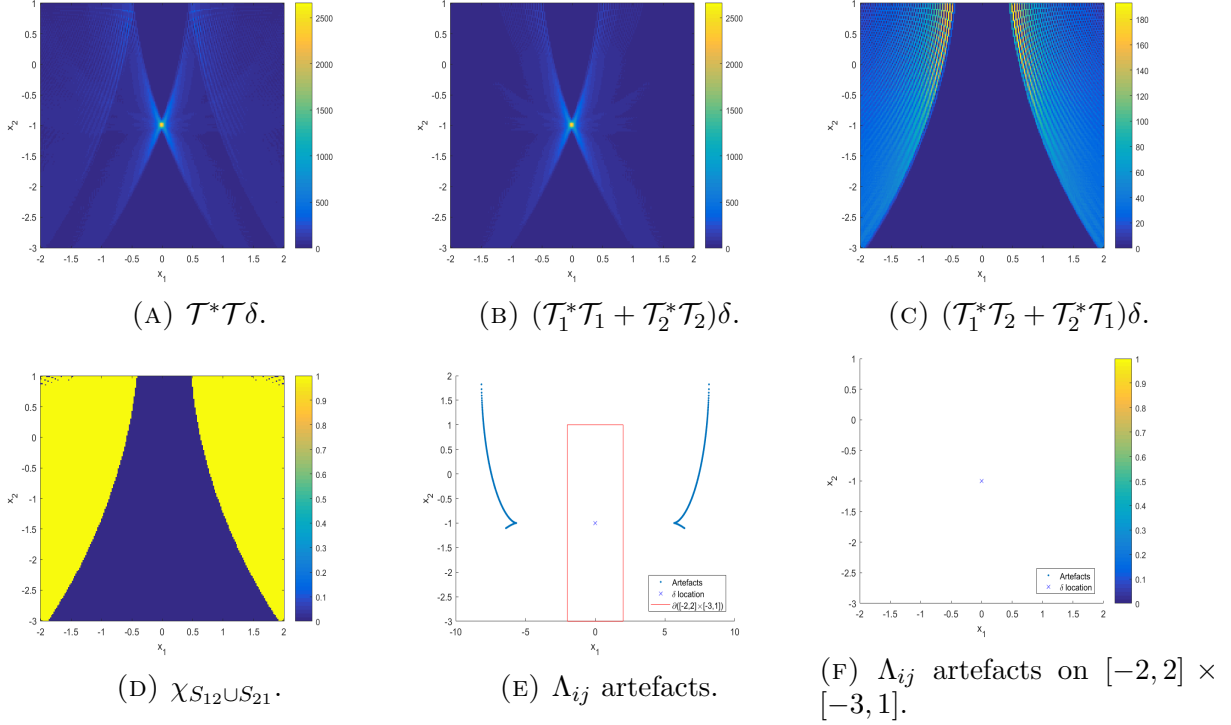


FIGURE 3.  $\mathcal{T}^*\mathcal{T}\delta$  (the  $\delta$  function is centered at  $\mathbf{O} = (0, -1)$ ) images with the predicted artefacts due to the limited data backprojection (on  $S_{12} \cup S_{21}$ ) and those induced by  $\Lambda_{12}$  and  $\Lambda_{21}$ .

where  $r = \frac{2-x_2}{\cos \beta}$ ,  $s = \sqrt{r^2 - 1}$  and  $x_0 = x_1 - s + r \sin \beta$ . Hence the only contributions to the backprojection from  $\mathcal{T}_1^*\mathcal{T}_2$  and  $\mathcal{T}_2^*\mathcal{T}_1$  are on the following sets:

$$(3.28) \quad S_{12} = \{\mathbf{x} : \exists \beta \in [-\beta_m, \beta_m] \text{ s.t. } |\mathbf{y} - \mathbf{c}_2(s, x_0)| = r\}$$

where  $r = \frac{2-x_2}{\cos \beta}$  and  $x_0 = x_1 + s + r \sin \beta$  and

$$(3.29) \quad S_{21} = \{\mathbf{x} : \exists \beta \in [-\beta_m, \beta_m] \text{ s.t. } |\mathbf{y} - \mathbf{c}_1(s, x_0)| = r\}.$$

where  $r = \frac{2-x_2}{\cos \beta}$  and  $x_0 = x_1 - s + r \sin \beta$ . This means that all  $\Lambda_{ij}$  artifacts will be in these sets. Note that besides the  $\Lambda_{ij}$  artifacts shown in figure 4e and 4f there are limited data artifacts caused by circles meeting  $\mathbf{y}$  of radius  $r_M$  (figures 4a-4c) and these are of higher strength in Sobolev norm.

To simulate a  $\delta$  function discretely we assign a value of 1 to nine neighbouring pixels in a 200–200 grid (which will represent  $[-2, 2] \times [-3, 1]$ ) and set all other pixel values to zero. Letting our discrete delta function be denoted by  $x_\delta$ , we approximate  $\mathcal{T}^*\mathcal{T}\delta \approx A^T A x_\delta$ , where  $A$  is the discrete form of  $\mathcal{T}$ . For comparison we show images of

$$(\mathcal{T}_1^*\mathcal{T}_2 + \mathcal{T}_2^*\mathcal{T}_1)\delta \approx (A_1^T A_2 + A_2^T A_1)x_\delta,$$

a characteristic function on the set  $S_{12} \cup S_{21}$ , and the artefacts induced by  $\lambda_{12}$  and  $\lambda_{21}$ . Here  $A_j$  is the discrete form of  $\mathcal{T}_j$ , for  $j = 1, 2$ . See figure 3. We see a butterfly wing type image artefacts in  $(A_1^T A_1 + A_2^T A_2)x_\delta$  due to the limited  $r$  and  $x_0$  inherent to our acquisition geometry (there are directions unresolved in the wavefront set of  $\delta$ ). In the  $(A_1^T A_2 + A_2^T A_1)x_\delta$  image we

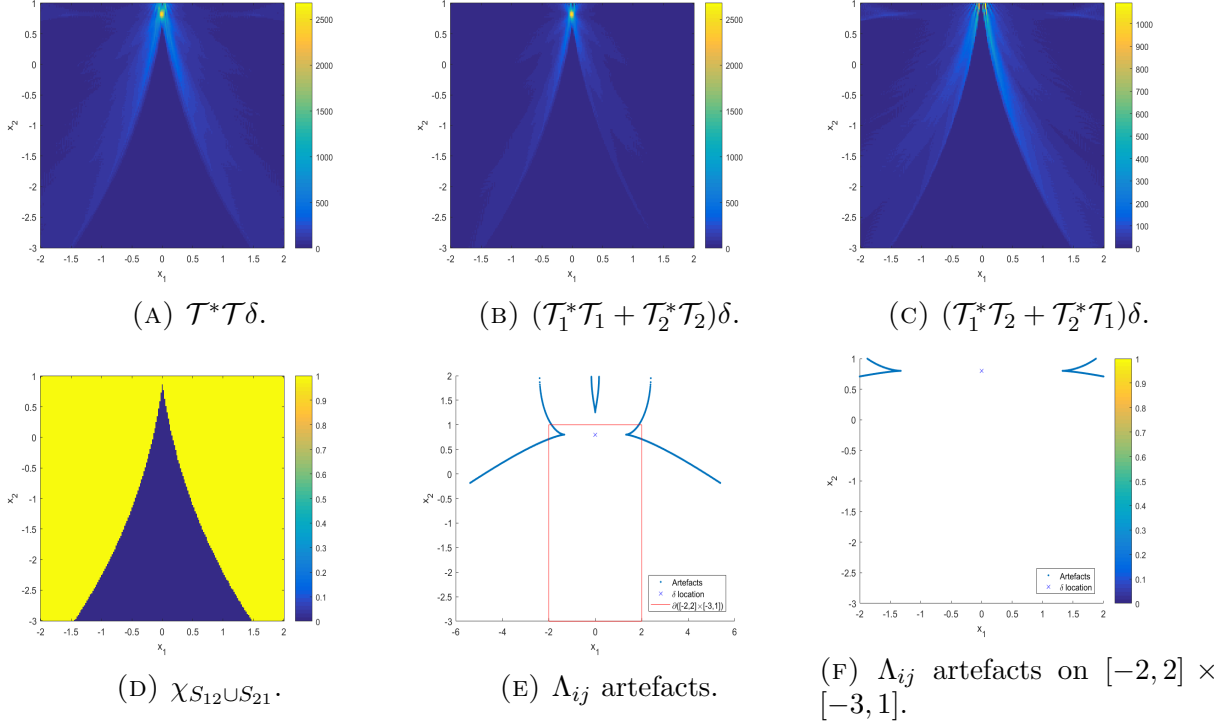


FIGURE 4.  $\mathcal{T}^* \mathcal{T} \delta$  (the  $\delta$  function is centered at  $(0, 0.9)$ ) images with the predicted artefacts due to the limited data backprojection (on  $S_{12} \cup S_{21}$ ) and those induced by  $\Lambda_{12}$  and  $\Lambda_{21}$ .

see artefacts appearing on the set  $S_{12} \cup S_{21}$  as predicted by our theory. The artefacts induced by  $\lambda_{12}$  and  $\lambda_{21}$  in this case lie outside the scanning region  $([-2, 2] \times [-3, 1])$ , and hence they are not observed in the reconstruction. In figure 4 however the artefact curves due to  $\lambda_{12}$  and  $\lambda_{21}$  intersect  $[-2, 2] \times [-3, 1]$  in the top left and right hand corners respectively. In this case the artefacts are observed faintly (their *magnitude* is small compared with the reconstructed delta function) in the reconstructions, and they align exactly with our predictions.

To show the artefacts induced by the  $\Lambda_{ij}$  more clearly, we repeat this analysis with a second derivative filtered backprojection. That is we show images of  $\mathcal{T}^* \frac{d^2}{dr^2} \mathcal{T} \delta$ . Note that the second derivative filter is applied in the variable  $r$  (the torus radius). The application of a second derivative filter is a common idea in lambda tomography [7, 8], and is known to highlight the image contours (singularities or image edges) in the reconstruction [36, Theorem 3.5]. See figure 5. As the artefacts induced by  $\Lambda_{ij}$  appeared to be largely outside the scanning region  $([-2, 2] \times [-3, 1])$  in our previous simulations, we have increased the scanning region size to  $[-3, 3] \times [-4, 2]$ , to show more the effects of the  $\Lambda_{ij}$  in the observed reconstruction. Here the filter  $\frac{d^2}{dr^2}$  suppresses the artefacts due to the limited data backprojection (on  $S_{12} \cup S_{21}$ ), and the artefacts induced by the  $\Lambda_{ij}$  appear as additional contours in the reconstruction. The observed artefacts appear most clearly in the  $(\mathcal{T}_1^* \frac{d^2}{dr^2} \mathcal{T}_2 + \mathcal{T}_2^* \frac{d^2}{dr^2} \mathcal{T}_1) \delta$  images in figure 5.

*Remark 3.5.* With precise knowledge of the locations of the artefacts induced by the  $\Lambda_{ij}$  we can assist in the design of the proposed parallel line scanner. That is we can choose  $a$ ,  $r_M$  and the scanning tunnel size to minimize the presence of the non-local artefacts in the



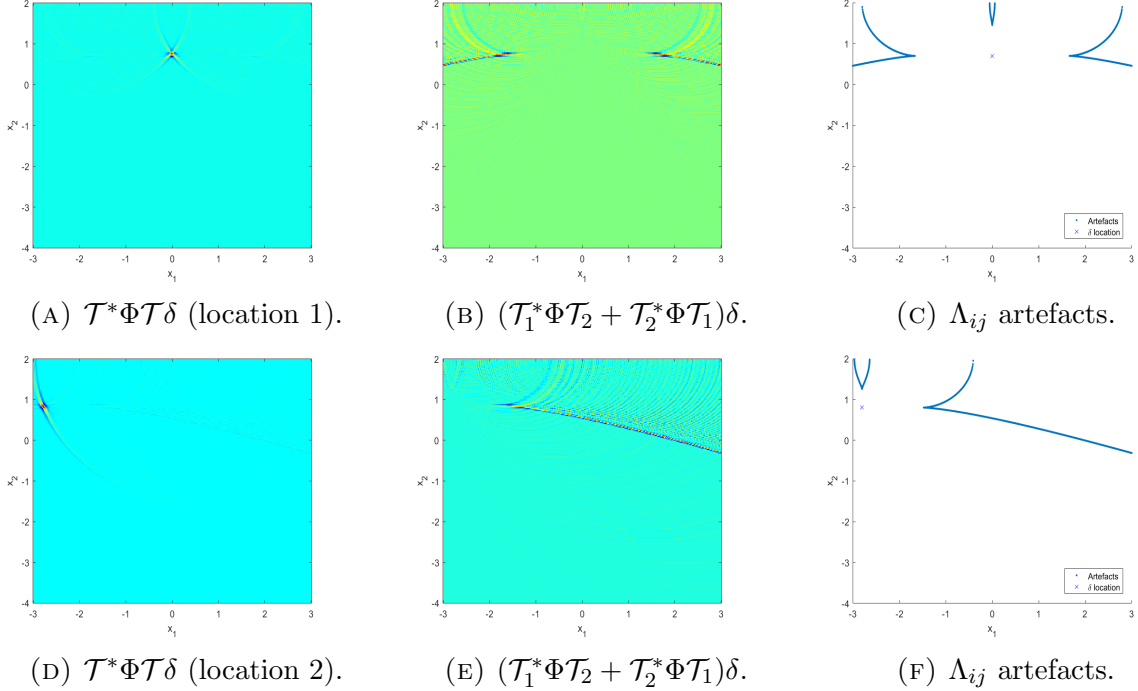


FIGURE 5.  $\mathcal{T}^*\Phi\mathcal{T}\delta$  and  $(\mathcal{T}_1^*\Phi\mathcal{T}_2 + \mathcal{T}_2^*\Phi\mathcal{T}_1)\delta$  images with the predicted artefacts induced by  $\Lambda_1$  and  $\Lambda_2$ . Here  $\Phi = \frac{d^2}{dr^2}$ . We give examples for two locations of  $\delta$  functions. Location 1 is  $(0,0.85)$  and location 2 is  $(-2.8,0.9)$ .

reconstruction (i.e., those from  $\Lambda_{ij}(f)$ ). Such advice would be of benefit to our industrial partners in airport screening to remove the concern for non-local artefacts in the image reconstruction of baggage. Indeed the machine dimensions used in this paper seem to be a suitable choice as the artefacts appear largely outside the reconstruction space (see figures 3 and 4).

#### 4. THE TRANSMISSION ARTEFACTS

The detector row  $D_C$  collects Compton (back) scattered data, which determine the data  $\mathcal{T}f(s, x_0)$  for a range of  $s$  and  $x_0$ , where  $f = n_e$  is the electron charge density. The forward detector array  $D_A$  collects transmission (standard X-ray CT) data, which determine a set of straight line integrals over the attenuation coefficient  $f = \mu_E$ , for some photon energy  $E$ . This limited data can cause artefacts in standard X-ray reconstructions, and we will analyze these artefacts using the theory in [2]. Let  $L_{s,\theta} = \{\mathbf{x} \in \mathbb{R}^2 : \mathbf{x} \cdot \Theta = s\}$  be the line parameterized by a rotation  $\theta \in [0, \pi]$  and a directed distance from the origin  $s \in \mathbb{R}$ . Here  $\Theta = (\cos \theta, \sin \theta)$  and  $L_{s,\theta}$  is the line containing  $s\Theta$  and perpendicular to  $\Theta$ .

In the scanning geometry of this article, the set  $S$  of X-ray transmitters is the segment between  $(-4, 3)$  and  $(4, 3)$  and the set of X-ray detectors,  $D_A$ , is the segment between  $(-4, -5)$  and  $(4, -5)$  as in figure 1. For this reason, the cutoff in the sinogram space is described by the set

$$(4.1) \quad H = \{(s, \theta) \in \mathbb{R} \times [-\pi/2, \pi/2] : L_{s,\theta} \cap S \neq \emptyset \text{ and } L_{s,\theta} \cap D_A \neq \emptyset\}.$$

The characteristic function on  $H$  is displayed in figure 6, and  $H$  appears as a diamond shape in the sinogram space.

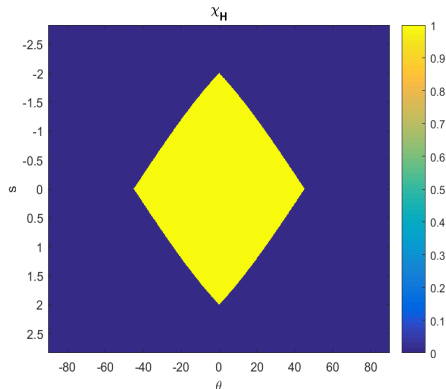


FIGURE 6. The characteristic function of  $H$ . Note that, in this picture, we are assuming the origin in object space is at  $\mathbf{O} = (0, -1)$  (the center of the square with opposite sides  $S$  and  $D_A$ ) when parameterizing lines.

To illustrate the added artifacts inherent in this incomplete data problem, we simulate reconstructions of delta functions with transmission CT data on  $H$ . We apply an both an unfiltered backprojection and a filtered backprojection. See figure 7. Here  $R_L f$  denotes  $Rf$  known for  $(s, \theta) \in H$ . By the theory in [2], artefacts caused by the incomplete data occur

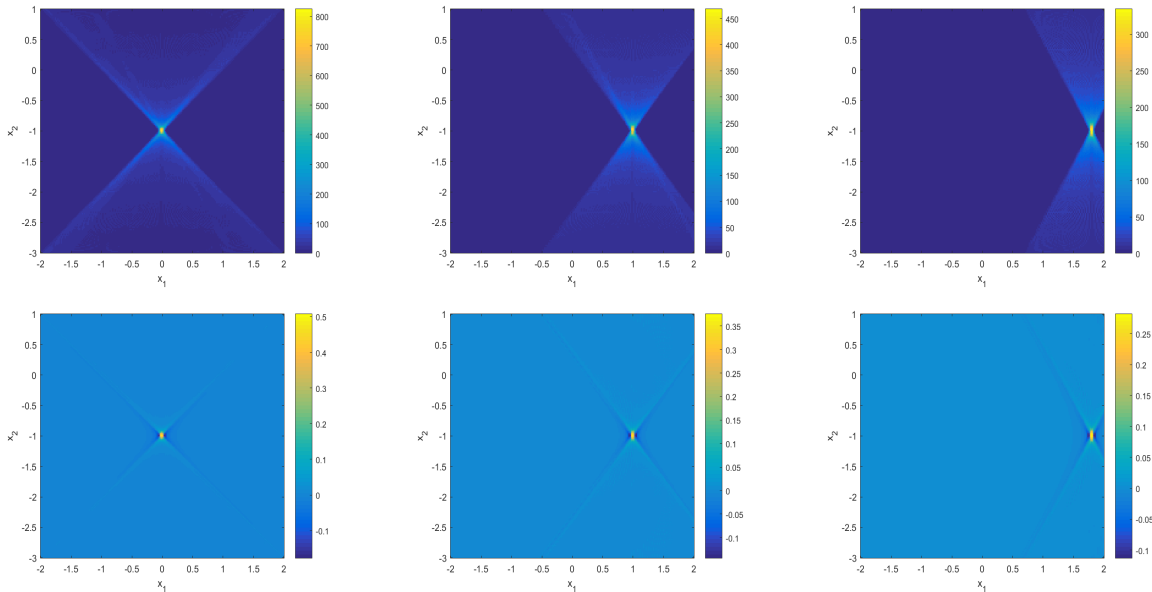


FIGURE 7. Top row –  $R_L^T R_L \delta_{(t,-1)}$  images at varying  $\delta$  function translations along the line  $x_2 = -1$ . Bottom row – reconstructions of these delta functions from  $R_L$  using the filtered backprojection formula.

on lines at the boundary of the data set—those for  $(s, \theta)$  in the boundary of  $H$ . Each delta function in Figure 7 is at a point  $(t, -1)$  for some  $t$  with  $0 < t < 2$ , so the lines that meet the

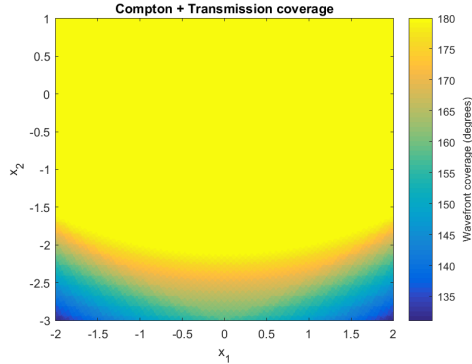


FIGURE 8. Picture of the range of wavefront directions that are visible at points in the reconstruction region  $[-2, 2] \times [-3, 1]$  from the joint data. The light (yellow) color in the top 3/4 of the figure indicates that all wavefront directions are visible from the joint data. The yellow region in which all wavefront directions are recovered will be called  $\Gamma$ . The darker (bluish) color near the bottom show that many directions are not visible for points near the bottom. Angles are measured from  $0^\circ =$  no coverage to  $360^\circ =$  full coverage.

support of the delta function,  $(t, -1)$  that are in the boundary of  $H$  must also contain either  $(4, 3)$  or  $(4, -5)$ . This is true because  $S$  and  $D_A$  are mirror images about the line  $y = -1$  and since  $t \in (0, 2)$ .

Furthermore, by this on symmetry, these artifact lines will be reflections of each other in the vertical line  $x_1 = t$ . This is illustrated in our reconstructions in Figure 7. The opening angle of the cone in the delta reconstructions decrease (fewer wavefront set directions are stably resolved) as we translate  $\delta$  to the right on the line  $x_1 = -1$ . The artefacts are also observed similarly in reconstructions using the Filtered Back Projection (FBP) formula, but the scale is different, so they are more difficult to see.

*Example 4.1.* We now use these ideas to analyze the visible wavefront directions for the joint problem. Let  $\mathcal{S} = [-4, 4] \times [-5, 3]$  be the square between  $S$  and  $D_A$  and let  $\mathbf{O} = (0, -1)$ , the center of  $\mathcal{S}$ . We consider wavefront at points  $(x_1, x_2) \in [-2, 2] \times [-3, 1]$  which is a square centered at  $\mathbf{O}$  and the region in which our simulated reconstructions are done.

By (4.1), lines in the data set must intersect both  $S$  and  $D_A$ , so lines through  $\mathbf{O}$  in the data set are all lines through  $\mathbf{O}$  that are more vertical than the diagonals of  $\mathcal{S}$ . Because visible wavefront directions are normal to lines in the X-ray CT data set [32], the wavefront directions which are resolved lie in the horizontal open cone between normals to these diagonals. Therefore, they are in the cone

$$C_R = \{\pm(\cos \alpha, \sin \alpha) : -\pi/4 < \alpha < \pi/4\}.$$

This is illustrated in figure 1.

An analysis of the singularities that are visible by the Compton data was done in section 3.1. For the point  $\mathbf{O}$ , the angle defined by (3.21) gives  $\beta_m = 1.23$  and the cone of visible directions given by (3.22) is the vertical cone with angles from the vertical between  $-\beta_m$  and  $\beta_m$  since the parameter  $r_M = 9$ . A calculation shows that  $2(\pi/4 + \beta_m) > \pi$  and this implies  $C_R \cup C_T = S^1$  and we have a full resolution of the image singularities at  $\mathbf{O}$ .

However, for points near the bottom  $x_2 = -3$ , there are invisible singularities that are not visible from either the Compton or X-ray data. For example, the vertical direction  $(0, 1)$  is not normal to any circle in the Compton data set at any point  $(0, x_2)$  for  $x_2 \in [-2.5, -3]$ . Figure 8 shows the points for which all wavefront directions are visible at those points (yellow color—roughly for points  $(x_1, x_2)$  for  $x_2 > -2$ ) and near the bottom of the reconstruction region, there are more missing directions.

We let  $\Gamma$  denote the solid light-colored (yellow) region (roughly the top 3/4 of the figure) in Figure 8 in which all wavefront directions are recovered.

## 5. A JOINT RECONSTRUCTION APPROACH AND RESULTS

In this section we detail our joint reconstruction scheme and lambda tomography regularization technique, and show the effectiveness of our methods in combatting the artefacts observed and predicted by our microlocal theory. We first explain the physical relationship

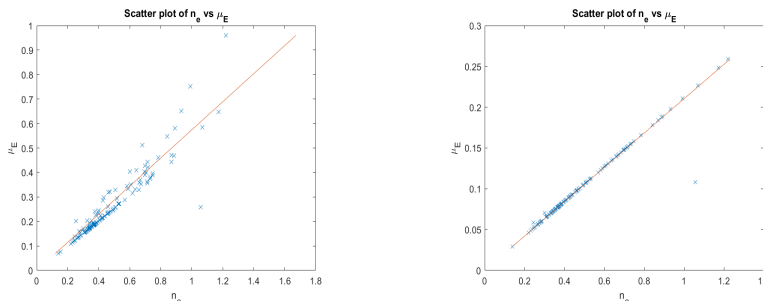


FIGURE 9. Scatter plot of  $n_e$  vs  $\mu_E$  for  $E = 100\text{keV}$  (left) and  $E = 1\text{MeV}$  (right), for 153 compounds with effective  $Z < 20$  taken from the NIST [22] database. The correlation is  $R=0.93$  (left) and  $R=0.98$  (right).

between  $\mu_E$  and  $n_e$ , which will be needed later in the formulation of our regularized inverse problem. The attenuation coefficient and electron density satisfy the formula [42, page 36]

$$(5.1) \quad \mu_E(Z) = n_e(Z)\sigma_E(Z),$$

where  $\sigma_E$  denotes the electron cross section, at energy  $E$ . Here  $Z$  denotes the effective atomic number. In the proposed application in airport baggage screening (among many other applications such as medical CT) we are typically interested in the materials with low effective  $Z$ . Hence we consider the materials with  $Z < 20$  in this paper. For large enough  $E$  and  $Z < 20$ ,  $\sigma_E(Z)$  is approximately constant as a function of  $Z$ . Equivalently  $\mu_E$  and  $n_E$  are approximately proportional for low  $Z$  and high  $E$  by equation 5.1. See figure 9. We see a strong correlation between  $n_e$  and  $\mu_E$  when  $E = 100\text{keV}$  and  $Z < 20$ , and even more so when  $E$  is increased to  $E = 1\text{MeV}$ . The sample of materials considered consists of 153 compounds (e.g. wax, soap, salt, sugar, the elements) taken from the NIST database [23]. In this case  $\sigma_E \approx \nu$  for some  $\nu \in \mathbb{R}$  is approximately constant and we have  $\mu_E \approx \nu n_e$ . For a given energy  $E$ ,  $\nu$  is the slope of the straight line fit as in figure 9. Throughout the rest of this paper, we set  $\nu$  as the slope of the straight line in the left hand of figure 9 (i.e.  $\nu \approx 0.57$ ), and present reconstructions of  $\mu_E$  for  $E = 100\text{keV}$ .

In sections 3 and 4 we discovered that the  $R_L\mu_E$  and  $\mathcal{T}n_e$  data provide complementary information regarding the detection and resolution of edges in an image. More specifically

the line integral data resolved singularities in an open cone  $C_R$  with central axis  $x_1$  and the toric section integral data resolved singularities in a cone  $C_T$  with central axis  $x_2$ . So the overlapping cones  $C_R \cup C_T$  give a greater coverage of  $S^1$  than when considered separately. In figures 3, 4 and 7, this theory was later verified through reconstructions of a delta functions by (un)filtered backprojection.

For a further example, let us consider a more complicated phantom than a delta function, one which is akin to densities considered later for testing our joint reconstruction and lambda regularization method. In figure 10 we have presented reconstructions of an image phantom  $f$  (with no noise) from  $R_L f$  (transmission data–middle figure) using FBP, and from  $\mathcal{T}f$  (Compton data–right figure) by an application of  $\mathcal{T}^* \frac{d^2}{dr^2}$  (a contour reconstruction). In the reconstruction from Compton data, we see that the image singularities are well resolved in the vertical direction ( $x_2$ ), and conversely in the horizontal direction ( $x_1$ ) in the reconstruction from transmission data. In the middle picture (reconstruction from  $R_L$ ), the visible singularities of the object are tangent to lines in the data set (normal wavefront set) and the artifacts are along lines at the end of the data set that are tangent to boundaries of the objects. In the right-hand reconstruction from Compton data, the visible boundaries are tangent to circles in the data set and the streaks are along circles at the end of the data set. Note that the visible boundaries in each picture complement each other and together, image the full objects. This is all as predicted by the theory of sections 3 and 4 (and is consistent with the theory in [2] and [9]) and highlights the complimentary nature of the Compton and transmission data in their ability to detect and resolve singularities.

Given the complimentary edge resolution capabilities of  $R_L \mu_E$  and  $\mathcal{T} n_e$ , and given the approximate linear relationship between  $\mu_E$  and  $n_e$ , we can devise a joint linear least squares reconstruction scheme with the aim to recover the image singularities stably in all directions in the  $n_e$  and  $\mu_E$  images simultaneously. To this end we employ ideas in lambda tomography

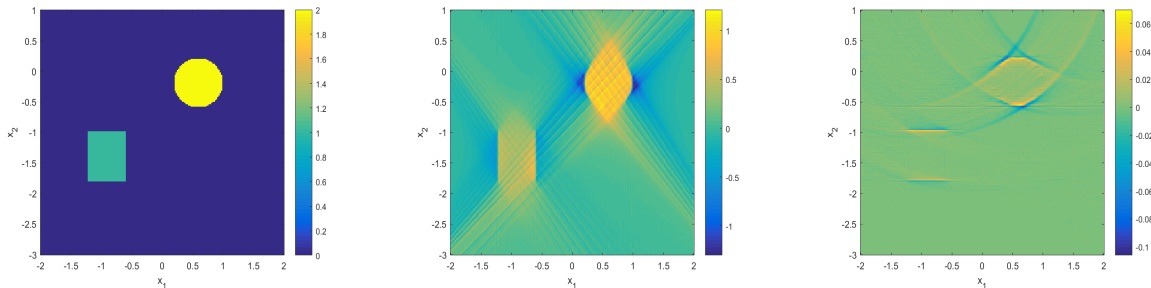


FIGURE 10. Image phantom  $f$  (left), a reconstruction from  $R_L f$  using FBP (middle) and  $\mathcal{T}^* \frac{d^2}{dr^2} \mathcal{T} f$  (right).

and microlocal analysis.

Let  $f \in \mathcal{E}(\mathbb{R}^n)$  and let  $Rf(s, \theta) = Rf_\theta(s) = \int_{L_{s,\theta}} f dl$  denote the hyperplane Radon transform of  $f$ , where  $L_{s,\theta}$  is as defined in section 4. The Radon projections  $Rf_\theta$  detect singularities in  $f$  in the direction  $\Theta = (\cos \theta, \sin \theta)$  (i.e. the elements  $(\mathbf{x}, \Theta) \in \text{WF}(f)$ ). Applying a derivative filter  $\frac{d^m}{ds^m} R_\theta$ , for some  $m \geq 1$ , increases the strength of the singularities in the  $\Theta$  direction by order  $m$  in Sobolev scale. Given  $f, g \in \mathcal{E}(\mathbb{R}^n)$ , we aim to enforce a similarity in  $\text{WF}(f)$  and  $\text{WF}(g)$  through the addition of the penalty term  $\|\frac{d^m}{ds^m} R(f - g)\|_{L^2(\mathbb{R} \times S^1)}$  to the least squares solution. Note that we are integrating over all directions

in  $S^1$  to enforce a full directional similarity in  $\text{WF}(f)$  and  $\text{WF}(g)$ . Specifically in our case  $f = \mu_E$ ,  $g = n_e$  and we aim to minimize the quadratic functional

$$(5.2) \quad \arg \min_{\mu_E, n_e} \left\| \begin{pmatrix} wR_L & 0 \\ 0 & \mathcal{T} \\ \alpha[\frac{d^m}{ds^m}R & -\nu\frac{d^m}{ds^m}R] \end{pmatrix} \begin{pmatrix} \mu_E \\ n_e \end{pmatrix} - \begin{pmatrix} wb_1 \\ b_2 \\ 0 \end{pmatrix} \right\|_2^2,$$

where  $R_L$  denotes a discrete, limited data Radon operator,  $R$  is the discrete form of the full data Radon operator,  $\mathcal{T}$  is the discrete form of the toric section transform,  $b_1$  is known transmission data and  $b_2$  is the Compton scattered data. Here  $\alpha$  is a regularization parameter which controls the level of similarity in the image wavefront sets. The lambda regularizers enforce the soft constraint that  $\mu_E = \nu n_e$  (since  $\frac{d^m}{ds^m}Rf = 0 \iff f = 0$  for  $f \in L_c^2(X)$ ), but with emphasis on the location, direction and magnitude of the image singularities in the comparison. Further we expect the lambda regularizers to have a smoothing effect given the nature of  $\frac{d^m}{ds^m}R$  as a differential operator (i.e. the inverse is a smoothing operation). Hence we expect  $\alpha$  to also act as a smoothing parameter. The weighting  $w = \|\mathcal{T}\|_2/\|R_L\|_2$  is included so as to give equal weighting to the transmission and scattering datasets in the inversion. We denote the joint reconstruction method using lambda tomography regularizers as ‘‘Jlam’’. A common choice for  $m$  in lambda tomography applications is  $m = 2$  [4, 36] (hence the name ‘‘lambda regularizers’’).

With complete X-ray data, the application of a Lambda term yields this  $R^* \frac{d^2}{ds^2} Rf = -4\pi\sqrt{-\Delta}f$  [25, Example 9], so the singularities of  $f$  are preserved and emphasized by order 1 in Sobolev scale, so they will dominate the Lambda reconstruction. Hence choosing  $m = 2$  is sufficient for a full recovery of the image singularities. Since the singularities are dominant in the lambda term, they are matched accurately in (5.2). Indeed we have already seen the effectiveness of such a filtering approach in recovering the image contours earlier in the right hand of figure 10. We find that setting  $m = 2$  here works well as a regularizer on synthetic image phantoms and simulated data with added pseudo random noise, as we shall now demonstrate. We note that the derivative filters for  $m \neq 2$  are also worth exploration but we leave such analysis for future work.

| $\mu_\epsilon \pm \sigma_\epsilon$ | Sep             | Jlam            | JTV             |
|------------------------------------|-----------------|-----------------|-----------------|
| $n_e$                              | $0.26 \pm .006$ | $0.14 \pm .004$ | $0.17 \pm .012$ |
| $\mu_E$                            | $0.41 \pm .02$  | $0.15 \pm .008$ | $0.17 \pm .022$ |

TABLE 1. Simple phantom mean ( $\mu_\epsilon$ ) and standard deviation ( $\sigma_\epsilon$ ) relative error comparison with separate reconstructions (Sep), joint reconstruction with lambda tomography regularizers (Jlam) and joint reconstruction with TV regularizers (JTV).

To test our reconstruction method, we first consider two test phantoms, one simple and one complex (as in [44]). The phantoms considered are supported on  $\Gamma$ , the region in figure 8 in which there is full wavefront coverage from joint X-ray and Compton scattered data. The simple density phantom consists of a rectangular and circular object with relative densities ( $n_e$ ) of 1 and 2 respectively (as displayed in the top left of figure 11). The complex density phantom consists of two ellipsoids, a right-angled-triangle and a thin cross, with relative densities of 1, 2, 3 and 4 respectively (as displayed in the top left of figure 12).

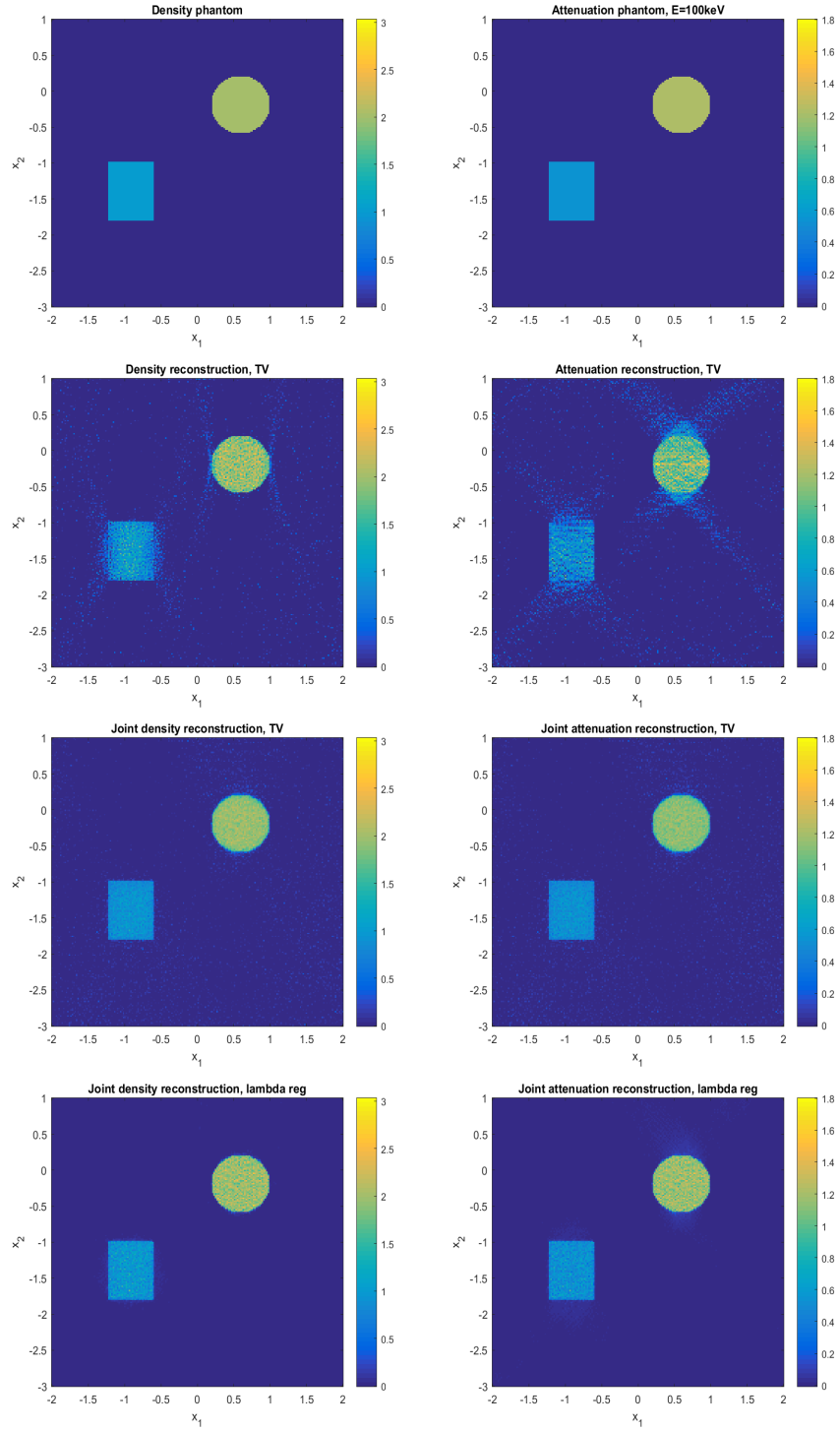


FIGURE 11. Simple phantom reconstructions, noise level  $\eta = 0.1$  (10%). Left column – density images, Right column – attenuation images. From top to bottom – the ground truth phantom and reconstructions using Sep, JTV and Jlam.

| $\mu_{\epsilon_A} \pm \sigma_{\epsilon_A}$ | Jlam           | JTV            |
|--|----------------|----------------|
| $n_e$                                      | $2.92 \pm .32$ | $8.38 \pm .60$ |
| $\mu_E$                                    | $2.15 \pm .70$ | $4.81 \pm .34$ |

TABLE 2. Simple phantom background (zeros of ground truth image) mean ( $\mu_{\epsilon_A}$ ) and standard deviation ( $\sigma_{\epsilon_A}$ ) absolute error comparison with Jlam and JTV.

| $\mu_\epsilon \pm \sigma_\epsilon$ (Jlam) | Squ             | Cir             |
|---|-----------------|-----------------|
| $n_e$                                     | $0.19 \pm .006$ | $0.12 \pm .004$ |
| $\mu_E$                                   | $0.20 \pm .01$  | $0.13 \pm .007$ |
| $\mu_\epsilon \pm \sigma_\epsilon$ (JTV)  | Squ             | Cir             |
| $n_e$                                     | $0.17 \pm .023$ | $0.11 \pm .019$ |
| $\mu_E$                                   | $0.17 \pm .024$ | $0.12 \pm .032$ |

TABLE 3. Simple phantom piecewise (non-zeros of ground truth image) mean ( $\mu_\epsilon$ ) and standard deviation ( $\sigma_\epsilon$ ) relative error comparison with Jlam and JTV. Top table – Jlam errors, Bottom table – JTV errors. Here Squ denotes the rectangular phantom and Cir denotes the circular phantom.

To simulate the corresponding attenuation coefficient phantoms, we multiply each of the non-zero components of the density image by  $\nu(1 + G)$ , where  $G$  is a random draw from  $\mathcal{N}(0, \sigma_{\text{err}})$  and  $\sigma_{\text{err}}$  is the standard deviation of the relative errors in the left hand straight line fit of figure 9 (for  $E = 100\text{keV}$ ). To simulate data we set

$$(5.3) \quad b = \begin{pmatrix} b_1 \\ b_2 \end{pmatrix} = \begin{pmatrix} R_L \mu_E \\ \mathcal{T} n_e \end{pmatrix}$$

and add a pseudo random Gaussian noise

$$(5.4) \quad b_\eta = b + \eta \|b\|_2 \frac{v_G}{\sqrt{l}},$$

for some noise level  $\eta$ , where  $l$  is the length of  $b$  and  $v_G$  is a vector of length  $l$  of draws from  $\mathcal{N}(0, 1)$ . For comparison we present separate reconstructions of  $\mu_E$  and  $n_e$  using Total Variation (TV regularizers). That is we will find

$$(5.5) \quad \arg \min_{\mu_E} \|R_L \mu_E - b_1\|_2^2 + \alpha \text{TV}(\mu_E)$$

to reconstruct  $\mu_E$  and

$$(5.6) \quad \arg \min_{n_e} \|\mathcal{T} n_e - b_2\|_2^2 + \alpha \text{TV}(n_e)$$

for  $n_e$ , where  $\text{TV}(f) = \|\nabla f\|_1$  and  $\alpha > 0$  is a regularization parameter. We will denote this method as ‘‘Sep’’. In addition we present reconstructions using a joint reconstruction method with TV (and denote this method as ‘‘JTV’’), for a comparison using joint data and the state-of-the-art regularization techniques. To implement JTV we minimize

$$(5.7) \quad \arg \min_{n_e} \left\| \begin{pmatrix} \nu(w R_L) \\ \mathcal{T} \end{pmatrix} n_e - \begin{pmatrix} w b_1 \\ b_2 \end{pmatrix} \right\|_2^2 + \alpha \text{TV}(n_e),$$



where  $w = \|\mathcal{T}\|_2/\|R_L\|_2$  as before, and we set  $\mu_E = \nu n_e$  after we have reconstructed  $n_e$ . Here we impose the hard constraint that  $\mu_E = \nu n_e$ . We choose to do this to compare Jlam against the optimal performance using JTV, as the hard equality constraint halves the number of unknowns (i.e. we are only reconstructing  $n_e$ , as opposed to  $n_e$  and  $\mu_E$  simultaneously) to be recovered when compared to the soft constraint formulation (i.e. using an additional penalty term such as  $\|\mu_E - \nu n_e\|_2$ ). Due to the nature of the lambda regularization penalty we cannot reduce the number of unknowns in this way using Jlam, which gives an advantage to JTV over Jlam in this sense. We wish to stress however that the comparison with JTV is included purely to illustrate the potential advantages (and disadvantages) of the lambda regularizers when compared to the state-of-the-art regularization techniques on the market. Namely is the improvement in image quality due to joint data, lambda regularizers or are they both beneficial? We are not claiming a state-of-the-art performance using Jlam, but our results show Jlam is competitive, and it is numerically easier to implement, requiring only least squares solvers. The Jlam reconstructions are no worse than JTV and the reconstructions in Figure 13 show that Jlam has fewer artifacts when there is not full wavefront coverage (when the object is not contained in  $\Gamma$ ).

| $\mu_\epsilon \pm \sigma_\epsilon$ | Sep             | Jlam            | JTV             |
|------------------------------------|-----------------|-----------------|-----------------|
| $n_e$                              | $0.35 \pm .002$ | $0.24 \pm .006$ | $0.24 \pm .01$  |
| $\mu_E$                            | $0.63 \pm .006$ | $0.28 \pm .01$  | $0.25 \pm .018$ |

TABLE 4. Complex phantom mean ( $\mu_\epsilon$ ) and standard deviation ( $\sigma_\epsilon$ ) relative error comparison with separate reconstructions (Sep), joint reconstruction with lambda tomography regularizers (Jlam) and joint reconstruction with TV regularizers (JTV).

| $\mu_{\epsilon_A} \pm \sigma_{\epsilon_A}$ | Jlam           | JTV            |
|--|----------------|----------------|
| $n_e$                                      | $8.36 \pm .53$ | $21.0 \pm .88$ |
| $\mu_E$                                    | $9.69 \pm .91$ | $12.1 \pm .51$ |

TABLE 5. Complex phantom background (zeros of ground truth image) mean ( $\mu_{\epsilon_A}$ ) and standard deviation ( $\sigma_{\epsilon_A}$ ) absolute error comparison with Jlam and JTV.

To minimize (5.2), we store the discrete forms of  $R_L$ ,  $R$  and  $\mathcal{T}$  as sparse matrices and apply the Conjugate Gradient Least Squares (CGLS) solvers of [16, 17] (specifically the “IRnnfcgls” code) with non-negativity constraints (since the physical quantities  $n_e$  and  $\mu_E$  are known a-priori to be non-negative). To solve equations (5.5), (5.6) and (5.7) we apply the heuristic least squares solvers of [16, 17] (specifically the “IRhtv” code) with TV penalties and non-negativity constraints. The relative reconstruction error  $\epsilon$  is calculated as  $\epsilon = \|\mathbf{x} - \mathbf{y}\|_2/\|\mathbf{x}\|_2$ , where  $\mathbf{x}$  is the ground truth image and  $\mathbf{y}$  is the reconstruction. The absolute reconstruction error is  $\epsilon_A = \|\mathbf{x} - \mathbf{y}\|_2$ . For all methods compared against we simulate data and added noise as in equations (5.3) and (5.4), and the noise level added for each simulation is  $\eta = 0.1$  (10% noise). Through experimentation we found that  $1 < \alpha < 100$  was a suitable range for the choice of hyperparameter for all methods. In all simulations conducted here we choose

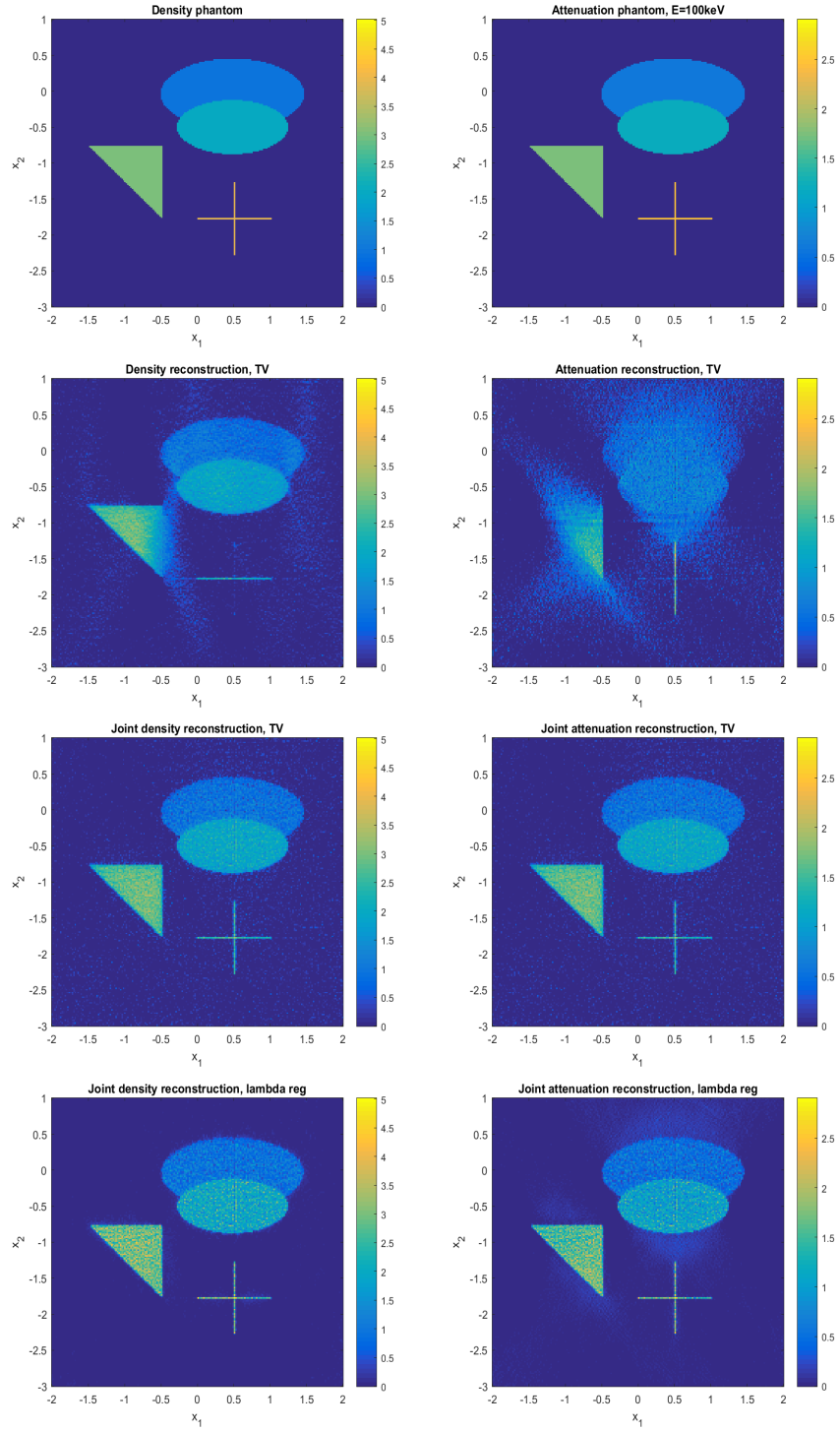


FIGURE 12. Complex phantom reconstructions, noise level  $\eta = 0.1$ . Left column – density images, Right column – attenuation images. From top to bottom – the ground truth phantom and reconstructions using Sep, JTV and Jlam.

|   |                 |                 |                 |                 |
|---|-----------------|-----------------|-----------------|-----------------|
| $\mu_\epsilon \pm \sigma_\epsilon$ (Jlam) | Ell1            | Ell2            | Tri             | Cro             |
| $n_e$                                     | $0.32 \pm .01$  | $0.23 \pm .006$ | $0.19 \pm .006$ | $0.36 \pm .043$ |
| $\mu_E$                                   | $0.36 \pm .024$ | $0.26 \pm .015$ | $0.22 \pm .015$ | $0.36 \pm .023$ |
| $\mu_\epsilon \pm \sigma_\epsilon$ (JTV)  | Ell1            | Ell2            | Tri             | Cro             |
| $n_e$                                     | $0.29 \pm .009$ | $0.16 \pm .01$  | $0.16 \pm .022$ | $0.42 \pm .039$ |
| $\mu_E$                                   | $0.31 \pm .04$  | $0.17 \pm .032$ | $0.15 \pm .029$ | $0.42 \pm .037$ |

TABLE 6. Complex phantom piecewise (non-zeros of ground truth image) mean ( $\mu_\epsilon$ ) and standard deviation ( $\sigma_\epsilon$ ) relative error comparison with Jlam and JTV. Top table – Jlam errors, Bottom table – JTV errors. Here Ell1 is the large ellipse, Ell2 is the smaller ellipse, Tri is the right-angled-triangle and Cro is the cross.

$\alpha \in \{j \in \mathbb{Z} : 1 \leq j \leq 100\}$  such that  $\epsilon$  is minimized (i.e. we are comparing the best possible performance of each method) for a noise level of  $\eta = 0.1$  (noting that the noise level remains constant throughout this paper). For each value of  $\alpha$  tested a different random 10% noise draw was used. After the optimal hyperparameters were selected, we performed 100 runs of Sep, Jlam and JTV on both phantoms for different added noise draws, and randomly generated attenuation phantoms (multiplying the non-zero densities by  $\nu(1 + G)$ , where  $G$  is a Gaussian draw as described earlier). We present the mean ( $\mu_\epsilon$ ) and standard deviation ( $\sigma_\epsilon$ ) relative errors over 100 runs in tables 1 and 4 for the simple and complex phantom respectively. For every table presented in this paper the results are given in the form  $\mu_\epsilon \pm \sigma_\epsilon$  for each method. The image reconstructions presented in this section are one of the 100 runs conducted selected at random.

See figure 11 for image reconstructions of the simple phantom using Sep, Jlam and JTV, and see table 1 for the corresponding mean and standard deviation of the reconstruction errors. In the separate reconstruction of  $n_e$  (using method Sep) we see a blurring of the ground truth image edges (wavefront directions) in the horizontal direction (the two vertical edges of the rectangle are not stably resolved and similarly for the circular phantom) and there are artefacts in the reconstruction due to limited data, as predicted by our microlocal theory. In section 3 we discovered the existence also of non-local artefacts induced by the mappings  $\lambda_{ij}$ . However these were found to lie largely outside the imaging space unless the singularity in question  $(\mathbf{x}, \xi) \in \text{WF}(n_e)$  were such that  $\mathbf{x}$  is close to the detector array (see figures 3 and 4). Hence why we do not see the effects of the  $\lambda_{ij}$  in the phantom reconstructions, as the phantoms are bounded sufficiently away from the detector array. The added regularization may smooth out such artefacts also, which was found to be the case in [44]. In the separate reconstruction of the attenuation coefficient image we see a similar effect, but in this case we fail to resolve the wavefront directions in the vertical direction due to limited line integral data. This is as predicted by the theory of section 4 and [2].

In the joint reconstruction results with TV and lambda regularizers (using methods JTV and Jlam) we see a large reduction of the image artefacts in the reconstructions of both  $n_e$  and  $\mu_E$  simultaneously, since with the joint data we are able to detect and stably resolve the image singularities in all directions. The reduction in the mean reconstruction error is also significant (particularly in the reconstruction of  $\mu_E$ ). Thus it seems that the joint data is the

greater contributor (over the lambda regularisation) to the improvement in the image quality (when the phantoms are supported on  $\Gamma$ ), as both approaches with joint data perform well and comparably.

The mean reconstruction error is further improved using Jlam on the simple phantom and we also see an improvement in the error standard deviation using Jlam. So on average we see better results in this case using Jlam, and the results are more consistent (less deviating from the mean), particularly in the case of the  $\mu_E$  reconstruction. Upon a side by side comparison of the Jlam and JTV image reconstructions, we see a comparable edge resolution. However there is a greater background distortion in the JTV image, whereas the zero regions are more accurately distinguished using Jlam. Conversely, the non-zero parts of the image are more effectively smoothed using JTV and less so with Jlam. This is validated by the results of tables 2, 3, 5 and 6, which compare the mean and standard deviation errors over the zero and non-zero parts of the phantoms separately. See tables 2 and 3 for the simple phantom error comparison and tables 5 and 6 for the complex phantom error comparison. Note that we are comparing the absolute error  $\epsilon_A$  on the phantom background (the zero part of the phantom), since the relative error  $\epsilon$  is undefined when comparing to zero. In addition we note that the JTV objective is non-linear and thus requires significant additional machinery (e.g. in the implementation of the ‘‘IRhtv’’ code of [12] used here for JTV) in the inversion when compared to Jlam, which is a straight forward implementation of linear least squares solvers.

For the complex phantom, see figure 12 for image reconstructions using Sep, Jlam and JTV,

| $\mu_\epsilon \pm \sigma_\epsilon$ | Jlam            | JTV             |
|------------------------------------|-----------------|-----------------|
| $n_e$                              | $0.09 \pm .008$ | $0.25 \pm .004$ |
| $\mu_E$                            | $0.11 \pm .017$ | $0.26 \pm .023$ |

TABLE 7. Horizontal bar phantom mean ( $\mu_\epsilon$ ) and standard deviation ( $\sigma_\epsilon$ ) relative error comparison with separate reconstructions (Sep), joint reconstruction with lambda tomography regularizers (Jlam) and joint reconstruction with TV regularizers (JTV).

| $\mu_{\epsilon_A} \pm \sigma_{\epsilon_A}$ | Jlam           | JTV            |
|--|----------------|----------------|
| $n_e$                                      | $1.17 \pm .14$ | $5.90 \pm .21$ |
| $\mu_E$                                    | $0.95 \pm .32$ | $3.38 \pm .11$ |

TABLE 8. Horizontal bar phantom background (zeros of ground truth image) mean ( $\mu_{\epsilon_A}$ ) and standard deviation ( $\sigma_{\epsilon_A}$ ) absolute error comparison with Jlam and JTV.

and table 4 for the mean and standard deviation of the error. Here we see similar image artefacts as in the simple phantom reconstructions. There are severe image artefacts using Sep due to limited data and the TV regularizers are not sufficient to combat the artefacts. The mean reconstruction errors are further amplified using all methods (when compared to the simple phantom case) due to the increase in the problem complexity. We do not encounter any significant reconstruction artefacts using Jlam or JTV, and the distortion effects of the simple phantom reconstructions are present here also. The mean errors in this case are

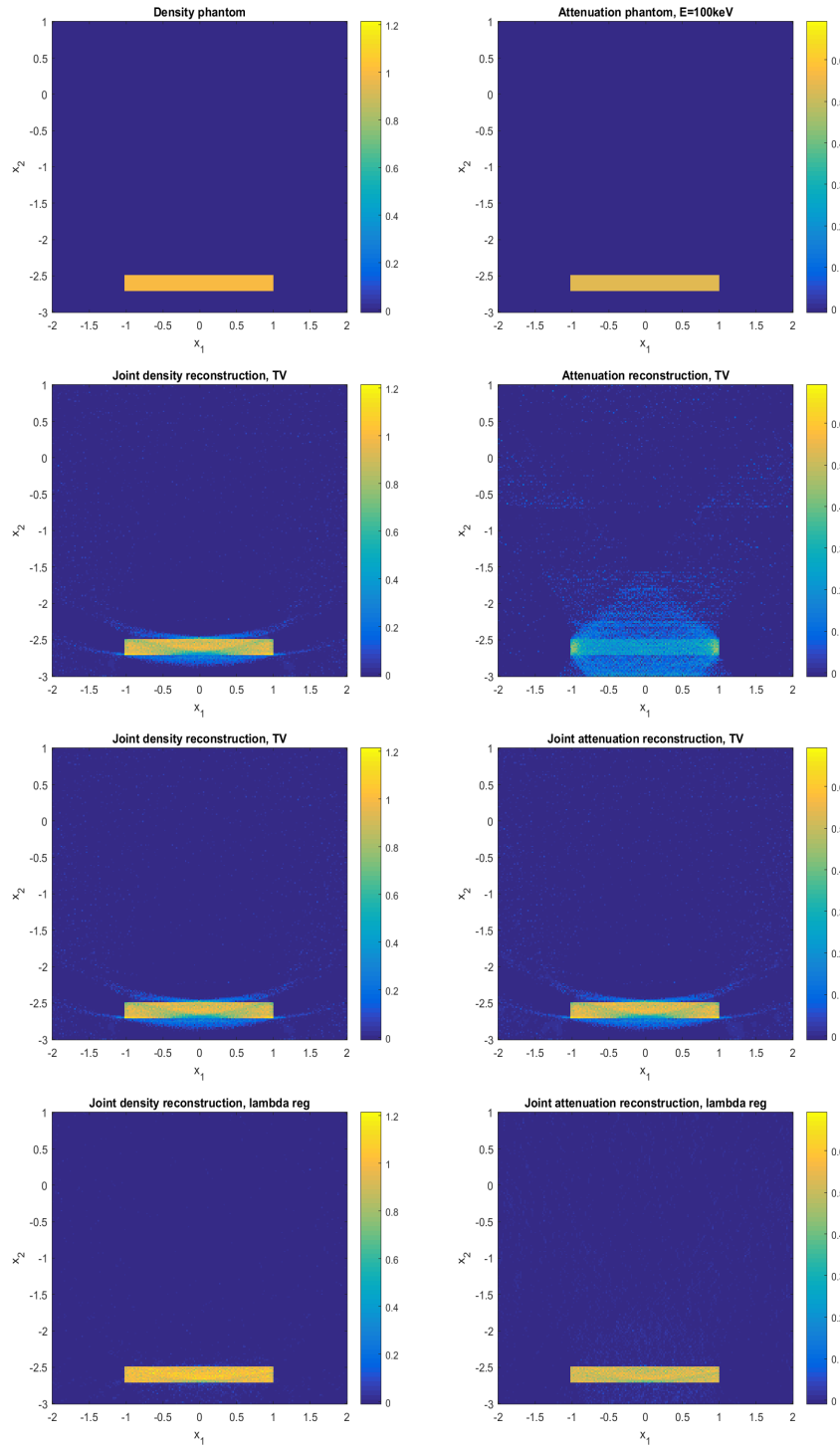


FIGURE 13. Horizontal bar phantom reconstructions, noise level  $\eta = 0.1$ . Left column – density images, Right column – attenuation images. From top to bottom – the ground truth phantom and reconstructions using Sep, JTV and Jlam.

improved using JTV, although again we notice a larger standard deviation in the error in the  $\mu_E$  image, as in the simple phantom case. So we can expect a less consistent result here also using JTV (when compared to Sep or Jlam) for varying attenuation phantoms. The simple

|   |                 |
|---|-----------------|
| $\mu_\epsilon \pm \sigma_\epsilon$ (Jlam) | Bar             |
| $n_e$                                     | $0.09 \pm .007$ |
| $\mu_E$                                   | $0.10 \pm .01$  |
| $\mu_\epsilon \pm \sigma_\epsilon$ (JTV)  | Bar             |
| $n_e$                                     | $0.18 \pm .009$ |
| $\mu_E$                                   | $0.19 \pm .037$ |

TABLE 9. Horizontal bar phantom piecewise (non-zeros of ground truth image) mean ( $\mu_\epsilon$ ) and standard deviation ( $\sigma_\epsilon$ ) relative error comparison with Jlam and JTV. Top table – Jlam errors, Bottom table – JTV errors.

and complex phantoms considered thus far are supported within  $\Gamma$  (the yellow region of figure 8) so as to allow for a full wavefront coverage in the reconstruction. To investigate what happens when the object is supported outside of  $\Gamma$ , we present additional reconstructions of a horizontal bar phantom with support towards the bottom (close to  $x_2 = -3$ ) of the reconstruction space. In this case we have limited data and the full wavefront coverage is not available with the combined X-ray and Compton data sets. The bar phantom and image reconstructions are presented in figure 13, and the relative errors are displayed in tables 7, 8 and 9. We present the relative errors for the two most competitive methods considered, namely Jlam and JTV. The reconstruction processes and hyperparameter selection applied here were exactly the same as for the simple and complex phantom. In this case we see artefacts in the Compton reconstruction along curves which follow the shape of the boundary of  $\Gamma$ , and the X-ray artefacts constitute a vertical blurring as before. The error and image quality when using the Jlam and JTV methods are less comparable in this example (when compared to the simple and complex phantom reconstructions) with Jlam out-performing JTV by all metrics considered. In particular JTV seems to fail to remove the curved artefacts observed in the Compton image. This gives evidence that Jlam is most optimal among the methods presented when faced with limited data, and further that Jlam can offer satisfactory reconstruction under such constraints. However this is only a single test of the capabilities of Jlam and JTV with limited data and we leave future work to conclude such analysis.

## 6. CONCLUSION

Here we have introduced new joint reconstruction and regularization techniques for low effective  $Z$  imaging ( $Z < 20$ ) based on ideas in microlocal analysis and lambda tomography. The reconstruction methods presented were tested on a “parallel line segment” (first introduced in [43]) acquisition geometry, motivated by system architectures for airport security screening applications. In section 3 we presented a novel microlocal analysis of the toric section transform  $\mathcal{T}$  first proposed in [43] for the Compton tomography problem, and proved the existence of non-local artefacts in a reconstruction of  $n_e$  from  $\mathcal{T}n_e$  through an analysis of the canonical relations of  $\mathcal{T}$ . We provided explicit expressions for the base points of the artefacts via the mappings  $\lambda_{12}$  and  $\lambda_{21}$ , and verified our predictions through a contour reconstruction of a delta function. The observed artefacts superimposed exactly with our

predictions, and the non-local artefacts appeared as additional (unwanted) image contours in the reconstruction. Further a microlocal analysis of the transmission tomography problem was provided in section 4. Here we showed that the missing data in the sinogram space formed a “diamond-shaped” smooth cutoff region and we explained the image artefacts in a reconstruction of  $\mu_E$  from the limited Radon data  $R_L\mu_E$  using the theory of [2].

By using microlocal analysis, we discovered that the transmission and Compton datasets provided complimentary information in terms of the image wavefront set recovery. That is the set of wavefront directions resolved by the transmission data were shown to be disjoint (or with only small angular intersection) from those covered by the Compton data (see Example 4.1). Using this idea and an approximate linear relationship between  $n_e$  and  $\mu_E$  (a high correlation in the NIST data [22] for high  $E$  and low  $Z$  effective), we devised a new linear least squares reconstruction scheme in section 5, which enforced a similarity in the image wavefront sets  $\text{WF}(n_e) \approx \text{WF}(\mu_E)$  by comparing the filtered Radon projections of  $n_e$  and  $\mu_E$ . Specifically we enforced a wavefront similarity by the addition of the penalty term  $\|\frac{d^m}{ds^m}R(\mu_E - n_e)\|_{L^2(\mathbb{R}\times S^1)}$ , where  $m \geq 1$  controls the order of the singularity compared. We set  $m = 2$  in our work, as is a common choice in lambda tomography applications [36]. We tested our reconstruction method (Jlam) on two image phantoms, one simple and one complex, and added a high level ( $\eta = 0.1$ , or 10% noise) of pseudo random noise to data generated by inverse crime. Image reconstructions and the relative error statistics were provided for Jlam and compared against a joint reconstruction with TV regularizers (method JTV) and reconstructions with separate data and TV regularizers (method Sep). We saw severe image artefacts appearing in the reconstructions with separate data (using Sep) due to limited data and the microlocal properties of  $R_L$  and  $\mathcal{T}$ . This was as predicted by the theory of sections 3 and 4. The image artefacts were almost completely removed however in the joint reconstructions and we saw a stable recovery of the image contours when using Jlam and JTV. The relative error statistics when using Jlam and JTV were also highly comparable. We note that the JTV objective is non-linear and thus requires significant additional numerical machinery when compared to Jlam, which is a straight forward implementation of linear least squares solvers. We also note that Jlam has fewer artifacts than JTV in our reconstructions in which not all wavefront is covered by the joint data (see in figure 13).

This work highlights the potential benefits of combining the scattered and transmission data (in certain acquisition geometries) from a microlocal perspective, in regards to the contour reconstruction of the density and attenuation coefficient. The new lambda regularizers and joint reconstruction techniques proposed (method Jlam) also show great promise moving forward and can perhaps be combined with TV ideas (or other such powerful regularizers) in future work to further improve the image quality.

We have focused on the parallel line scanner geometry of figure 1 in this work, which has a potential for application in airport baggage screening. While this is a motivated example which highlights the benefits of joint data in contour reconstruction, there are perhaps other machine geometries and applications where the proposed methods would offer improved results (compared to standard X-ray CT). In future work we aim to consider more generally the possible source-detector configurations for which the transmission and scattered data offer complimentary edge recovery. Another motivated example of interest is in limited angle fan-beam tomography. That is, can we add additional energy-resolved detectors to the classical fan beam setup such that the Compton data recovers the missing contours due to

limited angles? As the Compton data can be measured simultaneously with the transmission data, we expect such ideas to be beneficial in reducing dosage in medical CT (i.e. achieving satisfactory image quality with limited angle measurements (and hence limited dose) and joint Compton data).

#### ACKNOWLEDGEMENTS

This material is based upon work supported by the U.S. Department of Homeland Security, Science and Technology Directorate, Office of University Programs, under Grant Award 2013-ST-061-ED0001. The views and conclusions contained in this document are those of the authors and should not be interpreted as necessarily representing the official policies, either expressed or implied, of the U.S. Department of Homeland Security. The work of the second author was partially supported by U.S. National Science Foundation grant DMS 1712207.

#### REFERENCES

- [1] A. Aghasi, I. Mendoza-Sanchez, E. L. Miller, C. A. Ramsburg, and L. M. Abriola. A geometric approach to joint inversion with applications to contaminant source zone characterization. *Inverse problems*, 29(11):115014, 2013.
- [2] L. Borg, J. Frikel, J. S. Jørgensen, and E. T. Quinto. Analyzing reconstruction artifacts from arbitrary incomplete x-ray ct data. *SIAM Journal on Imaging Sciences*, 11(4):2786–2814, 2018.
- [3] T. A. BUBBA, G. Kutyniok, M. Lassas, M. Maerz, W. Samek, S. Siltanen, and V. Srinivasan. Learning the invisible: A hybrid deep learning-shearlet framework for limited angle computed tomography. *Inverse Problems*, 2019.
- [4] A. S. Denisjuk. Inversion of the generalized Radon transform. In *Applied problems of Radon transform*, volume 162 of *Amer. Math. Soc. Transl. Ser. 2*, pages 19–32. Amer. Math. Soc., Providence, RI, 1994.
- [5] J. J. Duistermaat. *Fourier integral operators*, volume 130 of *Progress in Mathematics*. Birkhäuser, Inc., Boston, MA, 1996.
- [6] J. J. Duistermaat and L. Hörmander. *Fourier integral operators*, volume 2. Springer, 1996.
- [7] A. Faridani, D. Finch, E. L. Ritman, and K. T. Smith. Local tomography, II. *SIAM J. Appl. Math.*, 57:1095–1127, 1997.
- [8] A. Faridani, E. L. Ritman, and K. T. Smith. Local tomography. *SIAM J. Appl. Math.*, 52:459–484, 1992.
- [9] J. Frikel and E. T. Quinto. Artifacts in incomplete data tomography with applications to photoacoustic tomography and sonar. *SIAM J. Appl. Math.*, 75(2):703–725, 2015.
- [10] L. A. Gallardo and M. A. Meju. Joint two-dimensional dc resistivity and seismic travel time inversion with cross-gradients constraints. *Journal of Geophysical Research: Solid Earth*, 109(B3), 2004.
- [11] L. A. Gallardo and M. A. Meju. Joint two-dimensional cross-gradient imaging of magnetotelluric and seismic traveltimes data for structural and lithological classification. *Geophysical Journal International*, 169(3):1261–1272, 2007.
- [12] S. Gazzola, P. C. Hansen, and J. G. Nagy. IR Tools: A MATLAB Package of Iterative Regularization Methods and Large-Scale Test Problems, 2017. arXiv preprint arXiv:1712.05602.
- [13] V. Guillemin and S. Sternberg. *Geometric Asymptotics*. American Mathematical Society, Providence, RI, 1977.
- [14] H. E. Guven, E. L. Miller, and R. O. Cleveland. Multi-parameter acoustic imaging of uniform objects in inhomogeneous soft tissue. *IEEE transactions on ultrasonics, ferroelectrics, and frequency control*, 59(8):1700–1712, 2012.
- [15] P. C. Hansen. *Rank-deficient and discrete ill-posed problems: numerical aspects of linear inversion*, volume 4. Siam, 2005.
- [16] P. C. Hansen. Regularization Tools version 4.0 for Matlab 7.3. *Numer. Algorithms*, 46(2):189–194, 2007.



- [17] P. C. Hansen and J. S. Jørgensen. AIR Tools II: algebraic iterative reconstruction methods, improved implementation. *Numer. Algorithms*, 79(1):107–137, 2018.
- [18] L. Hörmander. Fourier Integral Operators, I. *Acta Mathematica*, 127:79–183, 1971.
- [19] L. Hörmander. *The analysis of linear partial differential operators. I*. Classics in Mathematics. Springer-Verlag, Berlin, 2003. Distribution theory and Fourier analysis, Reprint of the second (1990) edition [Springer, Berlin].
- [20] L. Hörmander. *The analysis of linear partial differential operators. III*. Classics in Mathematics. Springer, Berlin, 2007. Pseudo-differential operators, Reprint of the 1994 edition.
- [21] L. Hörmander. *The analysis of linear partial differential operators. IV*. Classics in Mathematics. Springer-Verlag, Berlin, 2009. Fourier integral operators, Reprint of the 1994 edition.
- [22] J. Hubbell. Photon cross sections, attenuation coefficients and energy absorption coefficients. *National Bureau of Standards Report NSRDS-NBS29, Washington DC*, 1969.
- [23] J. H. Hubbell and S. M. Seltzer. Tables of x-ray mass attenuation coefficients and mass energy-absorption coefficients 1 keV to 20 MeV for elements  $Z=1$  to 92 and 48 additional substances of dosimetric interest. Technical report, National Inst. of Standards and Technology-PL, Gaithersburg, MD (United States), 1995.
- [24] W. A. Kalender. X-ray computed tomography. *Physics in Medicine & Biology*, 51(13):R29, 2006.
- [25] V. P. Krishnan and E. T. Quinto. Microlocal analysis in tomography. *Handbook of mathematical methods in imaging*, pages 1–50, 2014.
- [26] A. K. Louis. Combining Image Reconstruction and Image Analysis with an Application to Two-Dimensional Tomography. *SIAM J. Img. Sci.*, 1:188–208, 2008.
- [27] F. Natterer. *The mathematics of computerized tomography*. Classics in Mathematics. Society for Industrial and Applied Mathematics (SIAM), New York, 2001.
- [28] S. J. Norton. Compton scattering tomography. *Journal of applied physics*, 76(4):2007–2015, 1994.
- [29] V. Palamodov. An analytic reconstruction for the Compton scattering tomography in a plane. *Inverse Problems*, 27(12):125004, 2011.
- [30] V. P. Palamodov. A uniform reconstruction formula in integral geometry. *Inverse Problems*, 28(6):065014, 2012.
- [31] E. T. Quinto. The dependence of the generalized Radon transform on defining measures. *Trans. Amer. Math. Soc.*, 257:331–346, 1980.
- [32] E. T. Quinto. Singularities of the X-ray transform and limited data tomography in  $\mathbb{R}^2$  and  $\mathbb{R}^3$ . *SIAM J. Math. Anal.*, 24:1215–1225, 1993.
- [33] E. T. Quinto and O. Öktem. Local tomography in electron microscopy. *SIAM J. Appl. Math.*, 68:1282–1303, 2008.
- [34] H. Rezaee, B. Tracey, and E. L. Miller. On the fusion of Compton scatter and attenuation data for limited-view x-ray tomographic applications. *arXiv preprint arXiv:1707.01530*, 2017.
- [35] G. Rigaud. Compton scattering tomography: feature reconstruction and rotation-free modality. *SIAM J. Imaging Sci.*, 10(4):2217–2249, 2017.
- [36] G. Rigaud and B. N. Hahn. 3D Compton scattering imaging and contour reconstruction for a class of Radon transforms. *Inverse Problems*, 34(7):075004, 2018.
- [37] O. Semerci, N. Hao, M. E. Kilmer, and E. L. Miller. Tensor-based formulation and nuclear norm regularization for multienergy computed tomography. *IEEE Transactions on Image Processing*, 23(4):1678–1693, 2014.
- [38] O. Semerci and E. L. Miller. A parametric level-set approach to simultaneous object identification and background reconstruction for dual-energy computed tomography. *IEEE transactions on image processing*, 21(5):2719–2734, 2012.
- [39] B. H. Tracey and E. L. Miller. Stabilizing dual-energy x-ray computed tomography reconstructions using patch-based regularization. *Inverse Problems*, 31(10):105004, 2015.
- [40] T.-T. Truong and M. K. Nguyen. Compton scatter tomography in annular domains. *Inverse Problems*, 2019.
- [41] E. Vainberg, I. A. Kazak, and V. P. Kurozaev. Reconstruction of the internal three-dimensional structure of objects based on real-time integral projections. *Soviet Journal of Nondestructive Testing*, 17:415–423, 1981.

- [42] N. Wadson. *Modelling and correction of Scatter in a switched source multi-ring detector x-ray CT machine*. PhD thesis, The University of Manchester (United Kingdom), 2011.
- [43] J. Webber and E. Miller. Compton scattering tomography in translational geometries. Technical report, Tufts University, 2019.
- [44] J. Webber and E. T. Quinto. Microlocal analysis of a Compton tomography problem. *SIAM Journal on Imaging Sciences*, 2019. to appear.

## APPENDIX A. GENERATING THE PLOTS OF FIGURE 9

The generation of the plots of figure 9 is explained in more detail here. We will explain the generation of the plot for  $E = 100\text{keV}$ . Refer to figure 14. We first plotted  $\mu_E$  for  $E = 100\text{keV}$  against  $n_e$  for all materials in the NIST database [22] with effective  $Z$  less than 20. This is the left hand plot of figure 14. The set of materials with effective  $Z < 20$  was

$$Z_{\text{eff}} = \{Z : \sigma_E(Z) < \sigma_E(20), E = 100\text{keV}\},$$

where  $\sigma_E$  is the electron cross section. We noticed a large outlier (coal, or amorphous Carbon) which corrupts the correlation in our favour, and hence we chose to remove the material from consideration in simulation. The outlier is highlighted in the left hand plot. After the outlier was removed we noticed a number of materials located at the origin (with negligible attenuation coefficient and density, such as air) in the middle scatter plot of figure 14. As such materials again bias the correlation and plot standard deviation in our favour, these were removed to produce the left hand plot of figure 9 in the right hand of figure 14. The same points were removed in the generation of the right hand plot of figure 9 also, for  $E = 1\text{MeV}$ .

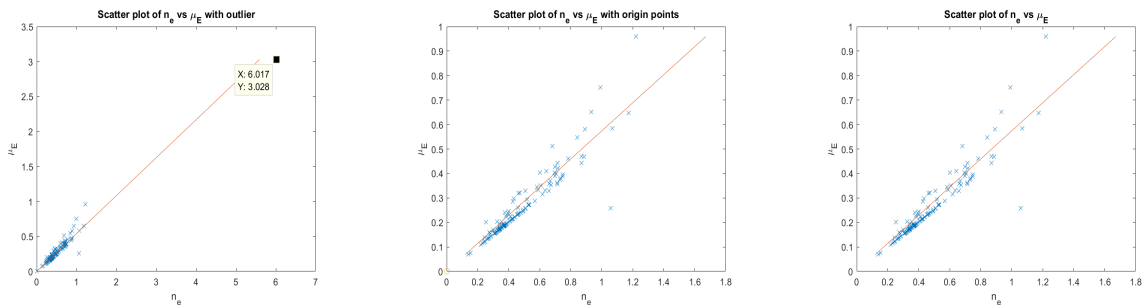


FIGURE 14. Scatter plot with outlier and origin points included (left,  $R=0.98$ ), scatter plot with the outlier removed and origin points included, the origin points highlighted by an orange circle (middle,  $R=0.95$ ), and the scatter plot of figure 9 with outliers and origin points removed (right,  $R=0.93$ ).

DEPARTMENT OF ELECTRICAL AND COMPUTER ENGINEERING, TUFTS UNIVERSITY, MEDFORD, MA USA

*E-mail address:* James.Webber@tufts.edu

DEPARTMENT OF MATHEMATICS, TUFTS UNIVERSITY, MEDFORD, MA USA

*E-mail address:* Todd.Quinto@tufts.edu

DEPARTMENT OF ELECTRICAL AND COMPUTER ENGINEERING, TUFTS UNIVERSITY, MEDFORD, MA USA

*E-mail address:* elmiller@ece.tufts.edu